Then, next step is to calculate the stator outer radius r_o. Firstly, the total slot area of all the stator slots A_{slot} can be written based on the winding electric loading A_e and the current density J_e:

$$A_{slot} = 2\pi(r_g + h_m)A_e/J_e S_{fg} \tag{39}$$

where S_{fg} is the slot fill factor. Meanwhile, the total slot area of all the stator slots A_{slot} can be also derived out using the structural parameters:

$$A_{slot} = \pi(r_g + h_m + h_1 + h_s)^2 - \pi(r_g + h_m + h_1)^2 - Z_s w_t h_s \tag{40}$$

Combining the Eqs. (39) and (40), the slot depth h_s can be determined. Then, the stator outer radius r_o can be given as:

$$r_o = r_g + h_m + h_1 + h_s + h_y \tag{41}$$

5.2 Rotor design

Defining the average flux density of each rotor yoke and middle of rotor tooth as B_{ry}, and B_{rt}, respectively, the rotor yoke thickness h_{ry} and rotor tooth width w_{rt} are able to be achieved using the similar derivation procedure as Eq. (35) and Eq. (36). Finally, the h_{ry} and w_{rt} are given as:

$$h_{ry} = r_g B_m / Z_r B_{ry} k_{stk} \tag{42}$$

$$w_{rt} = 4r_g B_m / Z_r k_{stk} B_{rt} \tag{43}$$

Then, the rotor slot depth h_{rs} is determined as:

$$h_{rs} = r_s + h_{ry} \tag{44}$$

6. Design methodology and evaluations

6.1 Design procedure

Based on the analytical equations and the investigations of key performances in the former parts, a quick and accurate analytical design of a FRPMM can be realized by following these procedures (as depicted in **Figure 27**):

1. Based on the performance investigations in **Figures 9–24**, the initial design values, including combination of stator slot and rotor slot number, electric loading, equivalent magnetic loading, airgap length, materials of active parts, etc. can be firstly selected.

2. Then, assuming an appropriate aspect ratio k_{lr}, the airgap radius r_g, and the stack length l_{stk} can be worked out using Eqs. (29) and (30).

3. Based on Eqs. (32–44), the detailed geometric parameters of the stator core and the rotor core are able to be obtained. Therefore, the stator outer diameter r_o and machine total length l_o can be finally determined.

4. After that, check if the stator outer diameter and the machine total length satisfy the required design specifications. If so, proceed to the FEA

verifications of machine performances. If not, reset the initial values such as combination of stator slot and rotor slot number, electric loading, equivalent magnetic loading, etc.
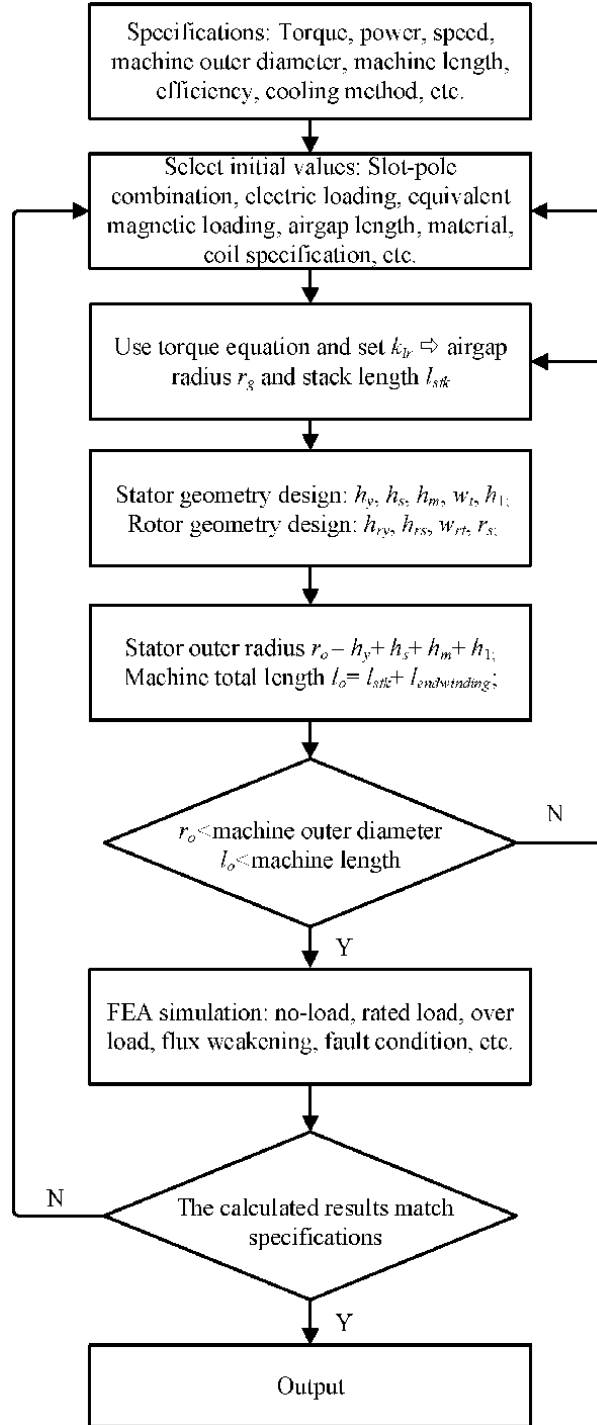

Figure 27.
Design flow of FRPMM.

5. Conducting FEA simulations, the electromagnetic performances such as back-EMF, average torque, pulsating torque, power factor, efficiency, etc. can be obtained. Check if all the performances satisfy the design specifications. If not, adjust the design parameters in the former steps and iterate the design flow until every output meets the requirement.

6. Finally, it is the result output.

6.2 Case study

In order show the effectiveness of the introduced analytical method, a FRPMM is designed based on the method. **Table 4** shows the specifications of the FRPMM, which mainly includes the rated torque, machine volume, cooling method, rated power, and speed. According to the rated torque, a design margin of 5% is suggested so as to make sure the torque output. Therefore, the requirement of the torque is 8.4 Nm for this design. Then, the combination of stator slots and rotor slots is determined in the first place. This combination is selected due to its high torque density and low pulsating torque, as shown in **Figure 13**. Then, since the cooling method is natural cooling, the electric loading and the equivalent magnetic loading are chosen as 300A/cm and 0.2 T, respectively. After that, based on the output torque value 8.4 Nm and Eq. (29), the airgap radius is determined as 38.5 mm. Furthermore, assuming the yoke flux density of stator core and rotor core as 1.0 T, and the teeth flux density of stator core and rotor core as 1.2 T, the detailed

Parameter	Value	Parameter	Value
Rated torque	8 Nm	Rated speed	300 rpm
Rotor inner diameter	32 mm	PM material	N38SH
Stator outer diameter	130 mm	Stack length	120 mm
Airgap length	0.6 mm	Iron material	50WW470
Cooling method	Natural cooling	Rated power	0.25 kW

Table 4.
Design specifications of a three-phase FRPMM.

	Parameter	Value	Parameter	Value
Stator	Outer diameter	124 mm	Inner diameter	79 mm
	Turns per phase	300	Teeth width	11.5 mm
	Slot number	12	Yoke thickness	6 mm
	Slot depth	13.5 mm	Yoke flux density	1.0 T
	Winding pole pair	1	Teeth flux density	1.1 T
Magnet	PM thickness	3 mm	Magnet width	7.8 mm
Rotor	Outer diameter	77.8 mm	Slot depth	10.4 mm
	Teeth flux density	1.2 T	Yoke thickness	12.5 mm
	Inner diameter	32 mm	Yoke flux density	1.0 T
	Teeth width	4 mm	Slot number	17

Table 5.
Design parameters of the FRPMM using the design method.

Parameter	Analytical design method	FEA
PM flux linkage	1.43 Wb	1.35 Wb
Back-EMF	44.8 V	42.4 V
Torque	8.4 Nm	7.97 Nm

Table 6.
Results comparison of the design method and 2D FEA.

Figure 28.
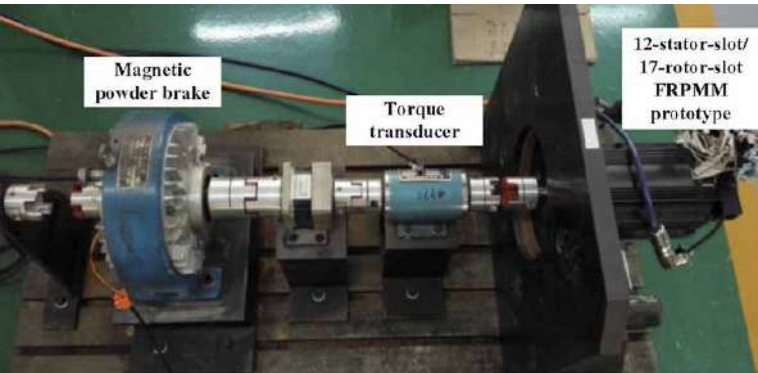*12-slot/17-pole FRPMM prototype: (a) stator; (b) rotor.*

Figure 29.
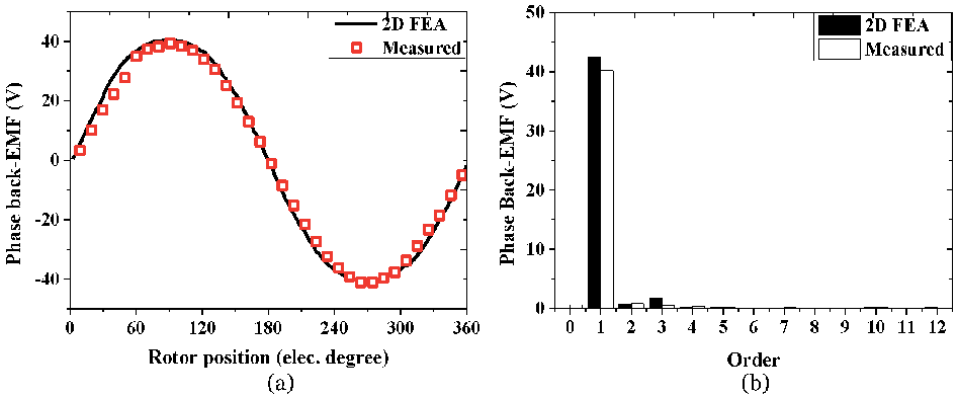*Test bed of the FRPMM prototype.*

Figure 30.
Back-EMF waveforms at rated speed 300 rpm: (a) waveform; (b) FFT analysis.

geometric parameters can all be determined. At last, the stator outer diameter is worked out as 124 mm, which is less than the requirement 130 mm. So far, this design is effective. **Table 5** summarizes the design parameters of the FRPMM. Finally, in order to verify the accuracy of the proposed analytical design method, the FEA model is built, and the simulated performances are compared to the analytical designed values. It can be seen in **Table 6** that the FEA simulated results match well with the analytical method. More importantly, the simulated performance output satisfies the design specifications. Therefore, this analytical design is successful.

6.3 Experimental study

To verify the calculated results by the analytical method and FEA, the FRPMM prototype has been built. Its major parameters are listed in **Table 4**. The structure and test bed of the prototype are shown in **Figures 28** and **29**, respectively.
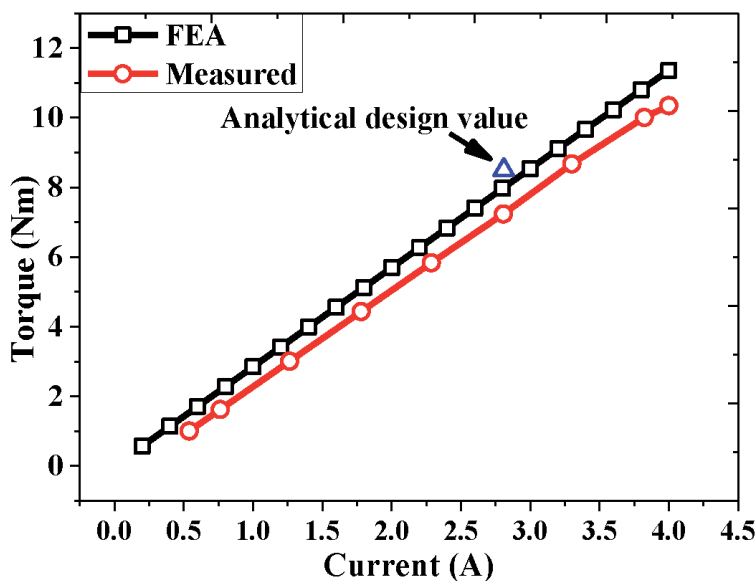

Figure 31.
Output torque vs. phase current.

Parameter	FEA	Experiment
Average torque at rated current	7.97 Nm	7.24 Nm
Torque per weight	0.66 Nm/kg	0.60 Nm/kg
Phase back-EMF magnitude at 300 rpm	42.4 V	41.2 V
THD of the phase back-EMF at 300 rpm	1.26%	2.63%
Total losses	99.5 W	116.7 W
Efficiency	60.3%	57.3%
Power factor	0.756	0.746

Table 7.
Result comparison of FEA and experiment of the FRPMM prototype.

Figure 30 compares the phase back-EMF waveform and spectrum at 300 rpm. It can be seen that the back-EMF waveforms are very sinusoidal. This is because the total harmonic distortion (THD) of FEA and experiments are only 1.26% and 2.63%, respectively. The sinusoidal back-EMF is inherent without any special design techniques such as skewing or pole shaping. Then, **Figure 31** shows the FEA simulated and experimental results of average torque at different winding current values. In addition, the analytical design value is also plotted as the blue triangle. It indicates that the simulated, analytical and experimental results have reached good agreements. Finally, **Table 7** compares the electromagnetic performances by FEA and experiments. Thus, the feasibility of the analytical design method can be seen.

7. Conclusions

The design of FRPMMs is usually based on time-stepping FEA, which are accurate but time-consuming. To save the design time meanwhile maintain the accuracy, this chapter proposes an analytical design method of FRPMMs. First, the sizing equation is derived, and then the dimensional parameters of stator and rotor are calculated. Finally, based on the above equations, an analytical design procedure is established. Moreover, in order to help to choose the initial design parameters in the sizing equation, including number of stator slots and rotor slots, airgap radius, electrical loading, and equivalent magnetic loading, their effects on the average torque, cogging torque, torque ripple, and power factor are investigated, providing reliable guidance for designers. At last, in order to make the introduced design methodology easier to understand, a FRPMM is designed and tested.

Acknowledgements

Nomenclature

B_r	remanent flux density
μ_r	relative permeability of magnets
g'	effective airgap length considering PM thickness
h_m	PM height along the magnetization direction
SO	stator slot opening ratio (=slot opening width/slot pitch)
g	airgap length
r_g	airgap radius
N_s	number of series turns per phase
P	number of stator winding pole pairs
l_{stk}	active stack length
Z_r	number of rotor teeth
ω_m	mechanical angular speed of rotor
Z_s	number of stator teeth
SPP	slot per pole per phase
θ	angular position of rotor axis with respect to the axis of phase *a*
θ_s	particular position in the stator reference frame measured from the axis of phase *a*
PR	pole ratio (=rotor pole number/winding pole pair)

Author details

Yuting Gao[1*] and Yang Liu[2]

1 Karlsruhe Institute of Technology, Karlsruhe, Germany

2 Wuhan Institute of Marine Electric Propulsion, Wuhan, China

*Address all correspondence to: gyt626890@gmail.com

IntechOpen

References

[1] Upadhyay P, Sheth NK, Rajagopal KP. Effect of rotor pole arc variation on the performane of flux reversal motor. In: International Conference on Electrical Machines and Systems. 2007. pp. 906-911

[2] Sheth NK, Rajagopal KR. Performance of flux reversal motor at various rotor pole arcs. In: International Conference on Electrical Machines and Systems. 2007. pp. 1517-1522

[3] Kushwaha D, Dwivedi A, Reddy R, et al. Study of 8/12 flux reversal machine as an alternator. In: Eighteenth National Power Systems Conference. 2014. pp. 1-4

[4] Shin HK, Kim TH, Kim CJ. Demagnetization characteristic analysis of inset-type flux-reversal machines. In: 15th International Conference on Electrical Machines and Systems. 2012. pp. 1-4

[5] Vandana R, Fernandes BG. Mitigation of voltage regulation problem in flux reversal machine. In: Energy Conversion Congress and Exposition. 2011. pp. 1549-1554

[6] More DS, Fernandes BG. Novel three phase flux reversal machine with full pitch winding. In: International Conference on Power Electronics. 2007. pp. 1007-1012

[7] Ahn J, Choi JH, Kim S, et al. Parametric variance consideration in speed control of single-phase flux reversal machine. IET Electric Power Applications. 2008;**2**(4):266-274

[8] Kim TH, Won SH, Lee J. Finite element analysis of flux-reversal machine considering BEMF current of a switch-off phase and v-i characteristics of a transistor and a freewheeling diode.

IEEE Transactions on Magnetics. 2006; **42**(4):1039-1042

[9] Wang C, Nasar SA, Boldea I. High speed control scheme of flux reversal machine. In: International Conference on Electric Machines and Drives. 1999. pp. 779-781

[10] Deodhar R, Andersson S, Boldea I, Miller T. The flux-reversal machine: A new brushless doubly-salient permanent-magnet machine. IEEE Transactions on Industry Applications. 1997;**33**(4):925-934

[11] Wang CX, Boldea I, Nasar SA. Characterization of three phase flux reversal machine as an automotive generator. IEEE Transactions on Energy Conversion. 2001;**16**(1):74-80

[12] Lee CHT, Chau KT, Liu C, et al. A new magnetless flux-reversal HTS machine for direct-drive application. IEEE Transactions on Applied Superconductivity. 2015;**25**(3):5203105

[13] Prakht V, Dmitrievskii V, Klimarev V, et al. High speed flux reversal motor for power tool. In: International Electric Drives Production Conference. 2016. pp. 306-311

[14] Bahrami H, Zabihi A, Joorabian M. A novel flux-reversal axial flux generator for high speed applications. International Conference on Power Electronics and Drives Systems. 2005;**2**: 1152-1155

[15] Prakht V, Prakht V, Sarapulov S, et al. A multipole single-phase SMC flux reversal motor for fans. In: International Conference on Electrical Machines. 2016. pp. 53-59

[16] Dmitrievskii V, Prakht V, Mikhalitsyn A. A new single-phase flux reversal motor with the cores made of

soft magnetic composite materials. In: International Conference on Electrical Machines and Systems. 2015. pp. 936-939

[17] Pellegrino G, Gerada C. Modeling of flux reversal machines for direct drive applications. In: European Conference on Power Electronics and Applications. 2011. pp. 1-10

[18] More DS, Kalluru H, Fernandes BG. Outer rotor flux reversal machine for rooftop wind generator. In: International Conference on IEEE Industry Application Society Annual Meeting. 2008. pp. 1-6

[19] Lee CHT, Chau KT, Liu C. Design and analysis of a cost-effective magnetless multiphase flux-reversal DC-field machine for wind power generation. IEEE Transactions on Energy Conversion. 2015;**30**(4): 1565-1573

[20] Li T, Sun Y, Li G, et al. Design of a novel double salient permanent magnet machine for wind power generation. In: International Conference on Electrical Machines and Systems. 2010. pp. 1053-1056

[21] Boldea I, Zhang L, Nasar SA. Theoretical characterization of flux reversal machine in low-speed servo drives-the pole-PM configuration. IEEE Transactions on Industry Applications. 2002;**38**(6):1549-1557

[22] Li W, Chau KT, Ching TW. A six-phase transverse-flux-reversal linear machine for low-speed reciprocating power generation. In: IEEE International Electric Machines and Drives Conference. 2015. pp. 618-623

[23] Gandhi A, Mohammadpour A, Sadeghi S. Doubled-sided FRLSM for long-stroke safety-critical applications. In: IEEE Industrial Electronics Society Annual Conference. 2011. pp. 4186-4191

[24] Chung S, Lee H, Sang M. A novel design of linear synchronous motor using FRM topology. IEEE Transactions on Magnetics. 2008;**44**(6):1514-1517

[25] Boldea I, Wang CX, Nasar SA. Design of a three-phase flux reversal machine. Electric Machines and Power Systems. 1999;**27**:849-863

[26] Kim TH, Lee J. A study of the design for the flux reversal machine. IEEE Transactions on Magnetics. July 2004; **40**(4):2053-2055

[27] Kim B, Lipo TA. Operation and design principles of a PM Vernier motor. IEEE Transactions on Industry Applications. March 2014;**50**(6): 3656-3663

[28] Gao Y, Qu R, Li D, et al. Design procedure of flux reversal permanent magnet machines. IEEE Transactions on Industry Applications. 2017;**53**(5): 4232-4241

[29] Zhu ZQ, Howe D. Instantaneous magnetic-field distribution in brushless permanent-magnet dc motors, Part III. Effect of stator slotting. IEEE Transactions on Magnetics. 1993;**29**(1): 143-151

[30] Gao Y, Qu R, Li D, et al. Torque performance analysis of three-phase flux reversal machines for electric vehicle propulsion. IEEE Transactions on Industry Applications. 2017;**53**(3): 2110-2119

Chapter 5

Predictive Direct Torque Control Strategy for Doubly Fed Induction Machine for Torque and Flux Ripple Minimization

Gopala Venu Madhav and Y.P. Obulesu

Abstract

The main drawback of Direct Torque Control (DTC) or Direct Power Control (DPC) is non-constant switching frequency; this drawback can be eliminated by employing predictive DTC. The predictive DTC technique is employed without much complicated online calculations by simply implementing constant switching times for active rotor voltage vectors to reduce torque and flux ripples and achieve constant switching frequency. The predictive DTC strategy has been implemented for RSC of Doubly Fed Induction Machine (DFIM). The performance of the proposed control methodology is compared with the classical DTC method under various operating conditions such as step change in torque, continuous variation of torque command, and the performance of DFIM near synchronous speed. It is found that the performance of the proposed predictive DTC strategy of DFIM is quite good compared to classical DTC strategy.

Keywords: predictive direct torque control, classical direct torque control, doubly fed induction machine, torque ripple, flux ripple

1. Introduction

In the field of renewable energy sources, wind energy is gaining much importance. The increase in the level of generation has two main restrictions, one is due to the limitations of the switching frequency of the power devices with respect to the power drive of the Doubly Fed Induction Machine (DFIM) and second one is the requirement of good dynamic torque performance, these restrictions are addressed by the proposed new Direct Torque Control (DTC) approach.

The foremost torque control methods proposed were classified into Field Oriented Control (FOC) techniques, Blaschke [1] and the direct control techniques. Then after, the concept of DTC, Takahashi and Ohmori [2] and Direct Self Control (DSC), Depenbrock [3] were introduced to achieve good steady-state and transient torque control conditions. Moreover, direct control techniques do not require current regulators, nor coordinate transformations or specific modulations like Pulse Width Modulation (PWM) or Space Vector Modulation (SVM) for pulse generation. The disadvantages are the lack of direct current control, torque control difficulties at very low speeds and especially variable switching frequency behavior.

The last important drawback put forward several authors in recent years, thus, methods like Direct Mean Torque Control (DMTC), [4] and Direct Torque Control based on Discrete Space Vector Modulation (DTC–DSVM), [5], have already achieved constant switching frequency. Furthermore, the methods proposed in Kang and Sul [6, 7] have extended the solution to reduce torque ripple at the same time imposing the switching frequency, as well as for different voltage-source multilevel topologies.

Further the concept of DTC have been applied to the brushless doubly fed induction machine, [8], or the equivalent Direct Power Control (DPC) strategy for several grid connected converter applications, [9].

In this paper, the analysis on the Doubly Fed Induction Machine (DFIM), which is a common solution for variable speed wind turbines, is discussed. The control methods like FOC have been performed by many authors, for example [10]. DTC and DPC methods without switching frequency imposition have also been carried out in Gomez & Amenedo [11], Datta & Ranganathan [12], while the DPC at constant switching frequency has also been developed in [13].

These mentioned direct control techniques that achieve constant switching frequency behavior are based on predictive control with a prediction horizon equal to one sample period. In this paper, predictive DTC technique for the DFIM will be employed based on [13] and the performance is compared with the DTC strategy, at constant switching frequency and with reduced torque and flux ripples criteria. This control technique is based on a prediction of the torque and the flux evolution of the DFIM. Hence, the new Predictive DTC (PDTC) strategy presented in this paper is based on a direct control of the electromagnetic torque and the rotor flux of the machine. Simulation results are presented and discussed, and at last, the results show that the predictive DTC technique presents good dynamic response compared to classical DTC concept.

In this Chapter, predictive DTC technique for the DFIM has been implemented and its performance is compared with the classical DTC of DFIM based on certain parameters like constant switching frequency, torque ripple and flux ripple. This control technique is based on a prediction of the torque and the flux evolution of the DFIM. To validate the proposed control scheme, results are presented. From these results, it is observed that the predictive DTC technique gives good dynamic response compared to classical DTC concept.

The control strategy even reduces the switching losses of the converter and reduces the electromagnetic torque and flux ripples at low switching frequency even under variable speed operating conditions.

In Section 1, the introduction of the Chapter is given.

In Section 2, Contributions and Novelty of this Chapter is explained.

In Section 3, Modeling of the DFIM is given.

In Section 4, the basic control principle of predictive DTC is explained and also implementation of the proposed predictive DTC strategy of DFIM along with selection of rotor voltage vectors for constant switching frequency and reduction of switching power losses are described.

In Section 5, Results are presented to validate the proposed control strategy.

In Section 6, the Conclusions of the Chapter are described.

In Section 7, the summary of the Chapter is given.

2. Contributions and novelty

The main contributions of this Chapter are as follows:

- Implementation of a new predictive Direct Torque Control (DTC) strategy of the Doubly Fed Induction Machine (DFIM) is presented which is designed to operate at a low constant switching frequency.

- The proposed DTC method effectively reduces the torque and flux ripples at low switching frequency, even under variable speed operation conditions.

- Results are presented to validate the proposed control strategy.

The novelty of this Chapter is that the predictive DTC have been developed to control the different parameters of DFIM, to improve its performance during transient, steady state, tracking behavior and operation near synchronous speed. All these cases are thoroughly investigated.

3. Modeling of DFIM

The DFIG model adopted is the qd0 rotating reference frame. It is because the model of DFIM is quite suitable with this frame of reference during transients. The transient solution of the DFIM model is possible because of the transformation from abc to qd0 by which the differential equations with time-varying inductances is converted into differential equations with constant inductances,

$$v_{qs} = R_s i_{qs} + \omega_s \psi_{ds} + \frac{d\psi_{qs}}{dt}$$

$$v_{ds} = R_s i_{ds} - \omega_s \psi_{qs} + \frac{d\psi_{ds}}{dt}$$

(1)

(or) simply (1) can be written as

$$\bar{v}_s^s = R_s \bar{i}_s^s + \frac{d\bar{\psi}_s^s}{dt}$$

(2)

Similarly, the q and d-axis rotor voltages referred to the stator are given by,

$$v_{qr}' = R_r' i_{qr}' + (\omega_s - \omega_r)\psi_{dr}' + \frac{d\psi_{qr}'}{dt}$$

$$v_{dr}' = R_r' i_{dr}' - (\omega_s - \omega_r)\psi_{qr}' + \frac{d\psi_{dr}'}{dt}$$

(3)

(or) simply (3) can be written as

$$\bar{v}_r^s = R_r \bar{i}_r^s + \frac{d\bar{\psi}_r^s}{dt} - j\omega_m \bar{\psi}_r^s$$

(4)

The stator and rotor fluxes can be calculated by using (5) and (6) can be used to calculate the magnitudes.

$$\overline{\Psi}_s = L_s \overline{I}_s + L_m \overline{I}_r$$

$$\overline{\Psi}_r = L_m \overline{I}_s + L_r \overline{I}_r \tag{5}$$

$$|\psi_s| = \sqrt{\psi_{ds}^2 + \psi_{qs}^2} \tag{6}$$

$$|\psi_r| = \sqrt{\psi_{dr}^2 + \psi_{qr}^2}$$

The electromagnetic torque of DFIM is given in (7).

$$T_{em} = \frac{3}{2} p Im\{\overline{\Psi}_s^{\wedge} . \overline{I}_s\} \ (or) \ \frac{3}{2} p \left(\psi_{s\alpha} i_{s\beta} - \psi_{s\beta} i_{s\alpha} \right)$$

$$(or) \ \frac{3}{2} p \left(\psi_{ds} i_{qs} - \psi_{qs} i_{ds} \right) (or) \approx \frac{3}{2} \frac{p}{2} L_m (i_{dr}' i_{qs} - i_{qr}' i_{ds}) \tag{7}$$

The active and reactive powers are given by:

$$P_s = \frac{3}{2} Re\{\vec{v} . \vec{i}^{\wedge}\} \ (or) \ \frac{3}{2} (v_\alpha i_\alpha + v_\beta i_\beta) \ (or) \ \frac{3}{2} (v_d i_d + v_q i_q) \overline{\Psi}_r = L_m \overline{I}_s + L_r \overline{I}_r$$

$$Q_s = \frac{3}{2} Im\{\vec{v} . \vec{i}^{\wedge}\}(or) \frac{3}{2} (v_\beta i_\alpha - v_\alpha i_\beta)(or) \frac{3}{2} (v_q i_d - v_d i_q) \tag{8}$$

4. Description of proposed predictive direct torque control strategy for torque and flux ripple minimization

The main drawback of classical DTC scheme is nonconstant switching behavior; it is avoided by the proposed predictive Direct Torque Control strategy. The constant switching behavior is achieved by increasing slightly the complexity of control strategy.

A sequence of three voltage vectors will be introduced at a constant switching period of which two are active vectors always followed by a zero vector, in order to reduce the ripples of both directly controlled variables compared to selection of four rotor voltage vectors depending on the position of rotor flux in classical DTC scheme. For that purpose, ripple reduction criteria based on a prediction of the electromagnetic torque and rotor flux evolution over time is implemented which is derived from (7) and (10) [13] and illustrated in **Figure 1(a)**.

The basic principles of the predictive DTC scheme are firstly, constant switching period 't$_s$' is defined. In predictive DTC, the control procedure is discretized unlike in DTC scheme, which is based on time domain. Secondly, at steady state condition, by taking the electromagnetic torque and flux amplitude errors to be minimized, the three different rotor voltage vectors are injected during t$_s$. Note that according to the chosen three vector sequence together with the specified time intervals for each vector, the electromagnetic torque and flux evolutions within the switching period can be different. Thirdly, this procedure is repeated at constant period t$_s$.

The Doubly Fed Induction Machine is modeled using (2), (4)–(6). The torque is calculated by using (7) in terms of complex conjugate of rotor flux and stator flux.
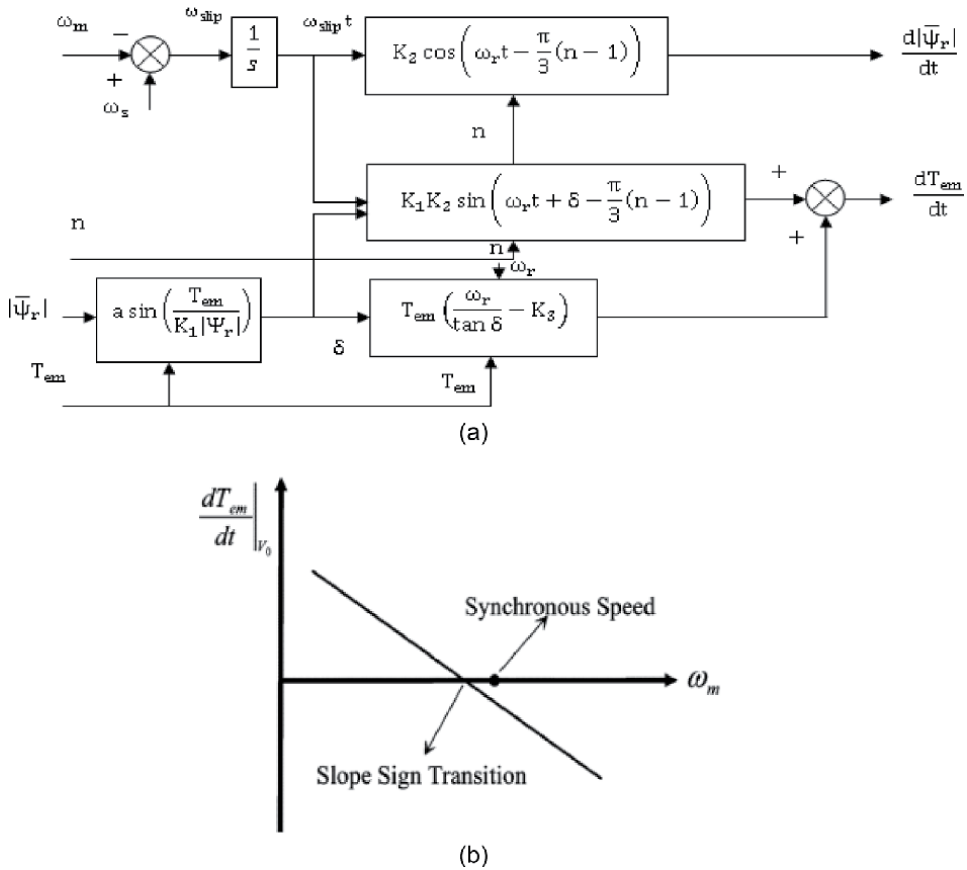
(a)

(b)

Figure 1.
(a) Simplified prediction scheme of torque and rotor flux of DFIM. (b) Variation of electromagnetic torque with zero vectors at constant torque and rotor flux.

4.1 Effect of voltage vector on the DFIM

Using (2), (4)–(7), the predictive expressions for torque and rotor flux are given by [2, 13]

$$\frac{d|\bar{\Psi}_r|}{dt} = \frac{1}{|\bar{\Psi}_r|}\left[\left(\frac{R_r L_m}{\sigma L_s L_r}\right)\text{Re}\{\bar{\Psi}_r \cdot \bar{\Psi}_s\} - \left(\frac{R_r}{\sigma L_r}\right)|\bar{\Psi}_r|^2 + \text{Re}\{\bar{\Psi}_r \cdot \bar{v}_r\}\right] \tag{9}$$

$$\frac{dT_{em}}{dt} = \frac{3}{2}P\frac{L_m}{\sigma L_s L_r}\left[\left(\frac{R_s}{\sigma L_s} + \frac{R_r}{\sigma L_r}\right)\text{Im}\{\bar{\Psi}_r \cdot \bar{\Psi}_s^{\wedge}\} - \omega_m\text{Re}\{\bar{\Psi}_r \cdot \bar{\Psi}_s\} + \text{Im}\{\bar{v}_s \cdot \bar{\Psi}_r^{\wedge}\} + \text{Im}\{\bar{\Psi}_s \cdot \bar{v}_r^{\wedge}\}\right] \tag{10}$$

The below space vector representations are used in order to analyze the expressions (9) and (10).

$$\bar{\Psi}_r = |\bar{\Psi}_r|e^{j\omega_s t} \tag{11}$$

$$\bar{\Psi}_s = |\bar{\Psi}_s|e^{j(\omega_s t + \delta)} \tag{12}$$

$$\bar{v}_s = |\bar{v}_s|e^{j\left(\omega_s t + \left(\frac{\pi}{2}\right) + \delta\right)} \tag{13}$$

$$\bar{v}_r = \frac{2}{3} V_{DC} e^{j(\omega_m t + \pi/3(n-1))} \tag{14}$$

where n is representation of sectors from 0 to 7. In (9), if Eqs. (11)–(14) are substituted, then

$$\frac{d|\bar{\psi}_r|}{dt} = \left[\left(\frac{R_r L_m}{\sigma L_s L_r} \right) |\bar{\psi}_s| \cos \delta - \left(\frac{R_r}{\sigma L_r} \right) |\bar{\psi}_r| + \frac{2}{3} V_{DC} \cos \left(\omega_{slip} t - \frac{\pi}{3}(n-1) \right) \right] \tag{15}$$

where

$$\omega_{slip} = \omega_s - \omega_m \tag{16}$$

Eq. (15) comprises of a cosine term and two constant terms, the cosine term with depends on DC bus voltage and it indicates that the cosine term of rotor flux variation is constant for zero vectors and only depends on active vectors.

Eq. (10) can be simplified considering the stator flux vector module which is nearly constant.

$$\frac{dT_{em}}{dt} = T_{em} \left(\frac{\omega_{slip}}{\tan \delta} - \left(\frac{R_s}{\sigma L_s} + \frac{R_r}{\sigma L_r} \right) \right) + p \frac{L_m}{\sigma L_s L_r} V_{DC} |\bar{\psi}_s| \sin \left(\omega_{slip} t + \delta - \frac{\pi}{3}(n-1) \right) \tag{17}$$

Eq. (17) is similar to rotor flux derivation with only one constant and one sine term.

Equations (15) and (17) are used practically as shown in **Figure 1(a)**, instead of (9) and (10). As shown in **Figure 1(a)**, the torque and flux derivatives depends on only four terms when considering the DC bus voltage, stator voltage and flux as constant magnitudes. In the expression (17), the constant term depends on T_{em} and, that means it depends on machine operating condition, which can be positive or negative as shown in **Figure 1(b)**. Because of this reason only, the phase shift order of each active vector varies, whereas, it is not like that for rotor flux derivative. The key point is knowing the slopes or the derivatives of torque and flux for each of the rotor voltage vector based on **Figure 1(a)** and **Table 1** and considering these slopes to be constants within the specific time in the given switching period, t_s, the torque and flux ripples can be maintained within the limits.

With constant values

$$K_1 = \frac{3}{2} p \frac{L_m}{\sigma L_s L_r} |\bar{\psi}_s| \tag{18}$$

$$K_2 = \frac{2}{3} V_{DC} \tag{19}$$

$$K_3 = \frac{R_s}{\sigma L_s} + \frac{R_r}{\sigma L_r} \tag{20}$$

From the **Figure 1(b)**, it can be seen that the slope of torque derivative varies proportionally to the slip speed provided at fixed torque and rotor flux operating conditions and also near synchronous speed, the slope of the zero vector becomes smaller obeying the fact that from the expression (17) the zero vector produce small

torque variation. This fact implies that near synchronous speed the amplitude of rotor voltage vector is small demanding the condition of zero vectors. As shown in **Figure 1(b)**, this transition from positive to negative torque slope is different to the synchronous speed.

4.2 Selection of first rotor voltage vector

The first vector is selected depending on the errors of torque and flux and the sector where the rotor flux lies, the look up table for vector selection is shown in **Table 1**. From the **Table 1**, it is noticed that the required rotor voltage vector should produce either positive or negative slope variation depending on the output of the torque or flux hysteresis comparators that is either 1 or −1, respectively.

4.3 Selection of second and third vector rotor voltage vector

The first vector is actually selected based on the classical DTC; the second vector is selected such that it is always followed by zero vectors in order to reduce the torque and flux ripples based on the predictive DTC strategy.

From **Figure 2**, it can be seen that from the derivative calculations block the required values of torque and flux evolutions depending on the each rotor voltage selected are fed to the ripple reduction criteria block, in which based on the slopes calculations by (15) and (17), the required rotor voltage vectors which are selected are active for the time period of this constant slopes. This constant time period of the constant slopes is fed to the switching table, where in the switching operation of rotor voltages are chosen in such a way that it reduces the switching losses.

From (15) and (17), it can be inferred that the rotor flux is constant for zero vector and it produces opposite sign for torque variation for first two active vectors. These two active vectors along with zero vectors are useful to control torque and rotor flux. By the two active vectors the rotor flux as one vector produce positive slope, the other vectors produce negative slope because of this the flux ripple is not eliminated completely as compared to torque ripple and further it affects the rotor and stator currents. **Table 2** shows the selection of second active vector, after the first active vector is selected. It clearly shows that, one vector cannot be selected, as the flux would have a very big or small variation, which leads to poor quality of flux output.

4.4 Reduction of switching power losses

The right choice of zero vectors V_0 and V_7 implies that there is reduction in switching power loss of the converter. Two different switching sequences exist for each pair of required active vectors, which allows the commutations of the converter to be reduced. **Table 3** shows the correct sequence of vectors, which allows only four commutations per switching period t_s. The candidate sequences are such

		Error of electromagnetic torque	
		1	**−1**
Error value of rotor flux	1	$V_{(n-1)}$	$V_{(n+1)}$
	−1	$V_{(n-2)}$	$V_{(n+2)}$
n = sector.			

Table 1.
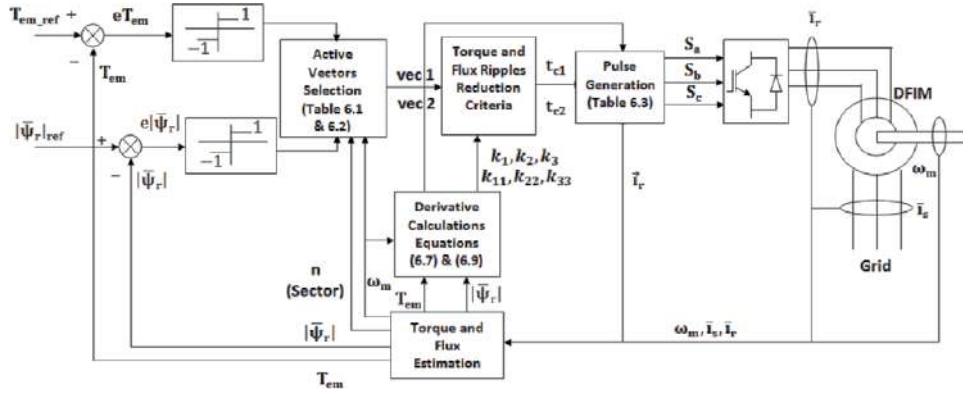*Selection of voltage vectors [13].*

Figure 2.
Block diagram of proposed predictive direct torque control strategy of DFIM.

	Active vectors
Below synchronous speed	$V_{(n+1)}$, $V_{(n+2)}$
Above synchronous speed	$V_{(n-1)}$, $V_{(n-2)}$

n = sector.

Table 2.
Selection of active vectors under steady-state [13].

Active vectors	Sector	Switching sequences	Zero vector
V_1-V_2	6(subs)	100-110-111	V_7
	3(hypers)	110-100-000	V_0
V_2-V_3	1(subs)	110-010-000	V_0
	4(hypers)	010-110-111	V_7
V_3-V_4	2(subs)	010-011-111	V_7
	5(hypers)	011-010-000	V_0
V_4-V_5	3(subs)	011-001-000	V_0
	6(hypers)	001-011-111	V_7
V_5-V_6	4(subs)	001-101-111	V_7
	1(hypers)	101-001-000	V_0
V_6-V_1	5(subs)	101-100-000	V_0
	2(hypers)	100-101-111	V_7

subs – sub synchronous speed operation, hypers – super synchronous speed operation.

Table 3.
Sequence of vector selection for reduction of switching power losses under steady-state [13].

that it reduces the switching power losses by transmitting the smallest current values, which is the main task of the proposed control strategy.

5. Results and discussion

The predictive DTC control scheme of DFIM has been implemented using MATLAB/Simulink. The specifications of DFIM are given in **Table 4**. The

Doubly fed induction machine	
Specifications	**Ratings**
Rated power	2.6 MW
Rated voltage	690 V
Synchronous speed	1500 rpm
Frequency	50 Hz
Number of pairs of poles	2
Stator to rotor turns ratio	0.34
Base voltage	398.4 V
Base current	2175 A
Base angular frequency	157 rads^{-1}
Base power	2.6 MW
Stator resistance	0.0108 pu
Stator leakage inductance	0.102 pu
Magnetizing inductance	3.362 pu
Rotor resistance referred to stator	0.0121 pu
Rotor leakage inductance referred to stator	0.11 pu
Inertia constant(H)	0.5 s
Friction coefficient(F)	0.05479 pu
DC-link capacitance	5e–3F
DC-link voltage	1200 V
Wind turbine	
Number of blades	3
Rotor diameter	70 m
Hub height	84.3 m
Turbine total Inertia	4.4532 e5Kgm^2
Stiffness constant (B)	2 pu
Mutual damping	1.5 pu
Cut-in wind speed	3 ms^{-1}
Cut-out wind speed	25 ms^{-1}
Rated wind speed	15 ms^{-1}

Table 4.
Specifications of DFIM and wind turbine.

conditions of steady state, transient, tracking behavior, and performance near synchronism of DFIM are examined, which are given in three subsections.

5.1 Transient and steady state analysis of DFIM

The performance of proposed control strategy of DFIM is analyzed for steady state and transient conditions. For the transient conditions, the step change in electromagnetic torque i.e., from −0.4 pu to +0.4 pu at 0.6 s is considered. That means, from generator mode (negative torque) to motoring mode (positive torque), with constant switching frequency of 1 kHz, with speed reference of 1350 rev/min, and DC-link voltage of 1200 V. The DFIM is under steady state

operation up to 0.6 s with torque of -0.4 pu and at 0.6 s the DFIM enters into transient state, and again it reaches its steady state value of 0.4 pu.

The response of stator currents in stationary reference frame are shown in **Figure 3(a)**. Therefore, there are two waveforms which refer to α, β components of stator currents. From the **Figure 3(a)**, it is observed that there are no over currents in stator, which indicates the effectiveness of the proposed control scheme even at sudden variation in torque demand. This is possible because of selection of proper rotor voltage vectors with their respective time intervals.

Figure 3(b) shows the response of developed torque for the proposed strategy and classical DTC strategy (not expressed in p.u. value), from the figure, it is noticed that the torque response of the DFIM closely followed the torque command and also torque ripple is zero.

From the **Figure 3(c)**, it can be seen that stator active power has good dynamic response when the reference torque is changed suddenly. From the figure, it is observed that the stator active power follows the torque demand to make the DFIM to develop the torque to match its reference value.

The response of the stator flux is shown in **Figure 3(d)**, from the figure, it is clearly noticed that the stator flux response remains constant which is not affected by variation in torque command.

The response of the rotor flux is shown in **Figure 3(e)**, from the figure, it is observed that the rotor flux response is also not affected by change in reference torque and also the rotor flux response is sinusoidal in nature which is not distorted due to sudden change in torque command.

Figure 3(f) shows response of the rotor speed of DFIM. From the **Figure 3(f)**, it is observed that there is decrease in rotor speed due to step change in reference torque but decrease in rotor speed is very small.

The response of rotor currents is shown in **Figure 3(g)**. From the **Figure 3(g)**, it is observed that there are no over currents in rotor, which indicates the effectiveness of the proposed control scheme even at sudden variation in torque demand. This is possible because of selection of proper rotor voltage vectors with their respective time intervals.

5.2 Performance analysis of DFIM during variable torque behavior

In this section, the proposed control scheme of DFIM is investigated for variable speed operation implying wind energy applications, and at the same instant, the torque reference may also vary respectively with speed of DFIM. This kind of behavior of wind energy system is called as tracking behavior. At this condition, the actual values of the DFIM should follow the reference values as closely as possible and this is clearly guaranteed by proposed control strategy which can be seen clearly through the results presented in this section. To explore the tracking behavior of DFIM, sinusoidally varying reference torque with amplitude of 0.4 pu and frequency of 3 Hz is set to the DFIM. By this set reference torque, the DFIM operates in generating and motoring modes. In this mode of operation, the other parameters of DFIM are same as mentioned in Section 5.1.

The predictive DTC strategy has good tracking behavior and it is confirmed that the reduction in torque and flux ripples is achieved as there are absolute absence of over currents and reduced ripples in stator currents as shown in **Figure 4(a)**. From the **Figure 4(a)**, it is noticed that there is continuous increase and decrease in the amplitude of stator currents for maintaining the consistency due to variable behavior of torque command. The stationary reference frame stator currents are clearly noticed in **Figure 4(a)**.
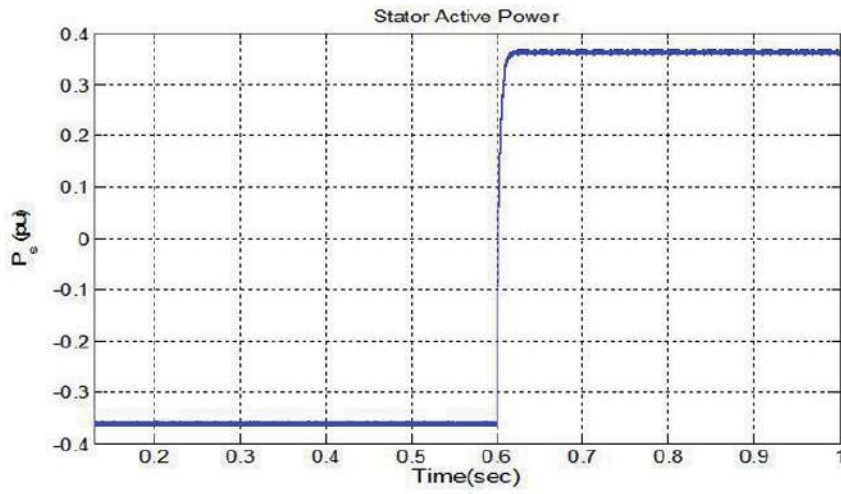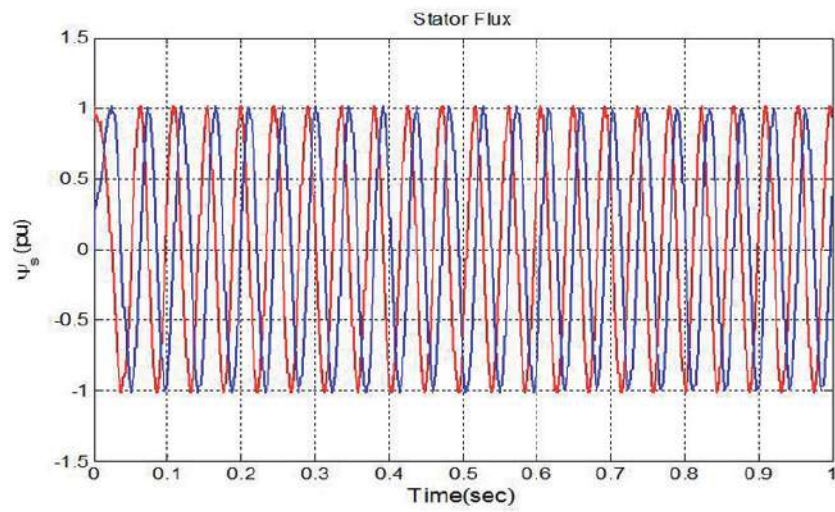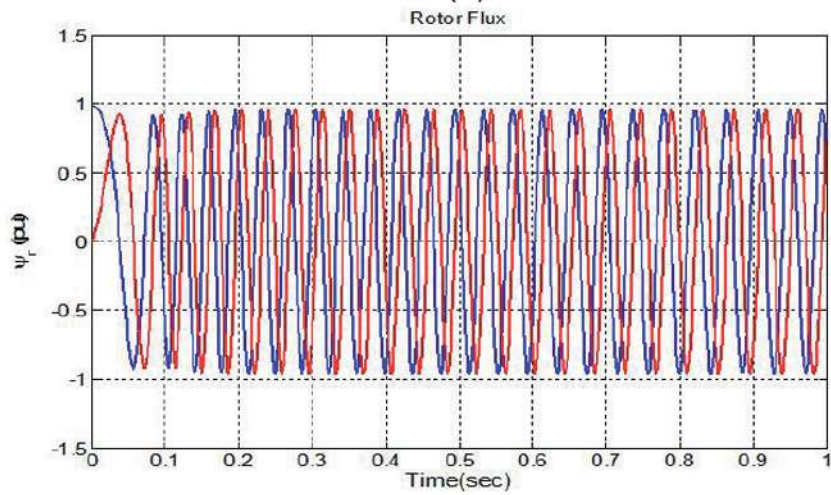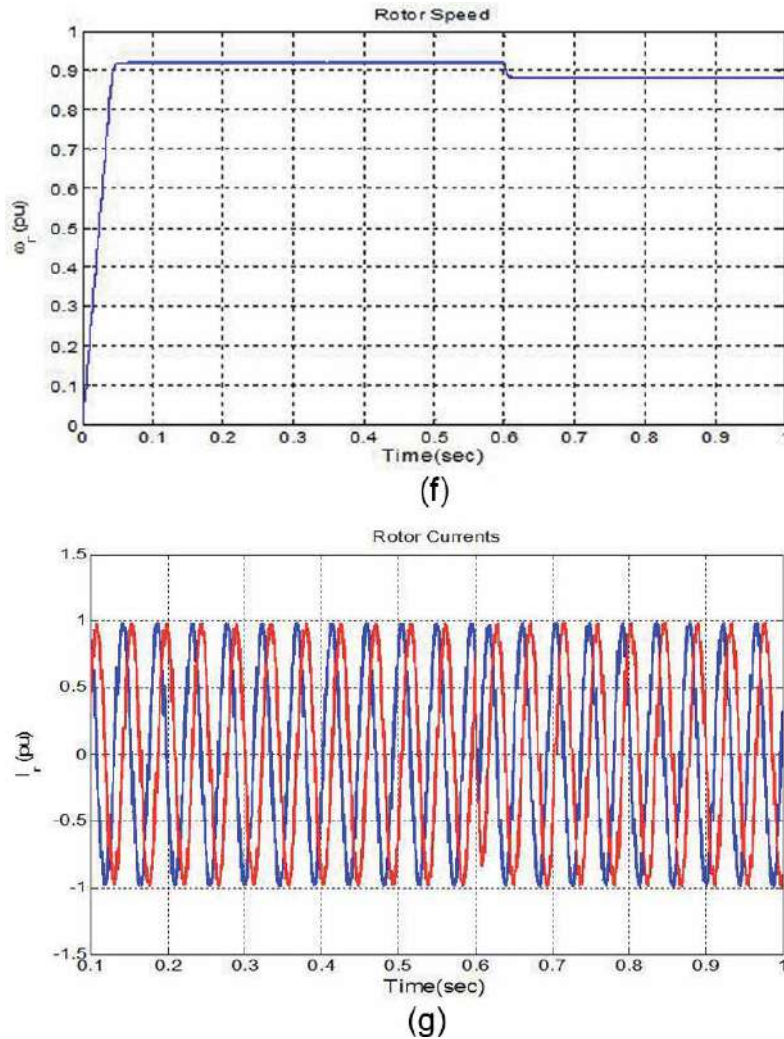
(a)

(i)

(ii)

(b)

(c)

(d)

(e)

Rotor Speed
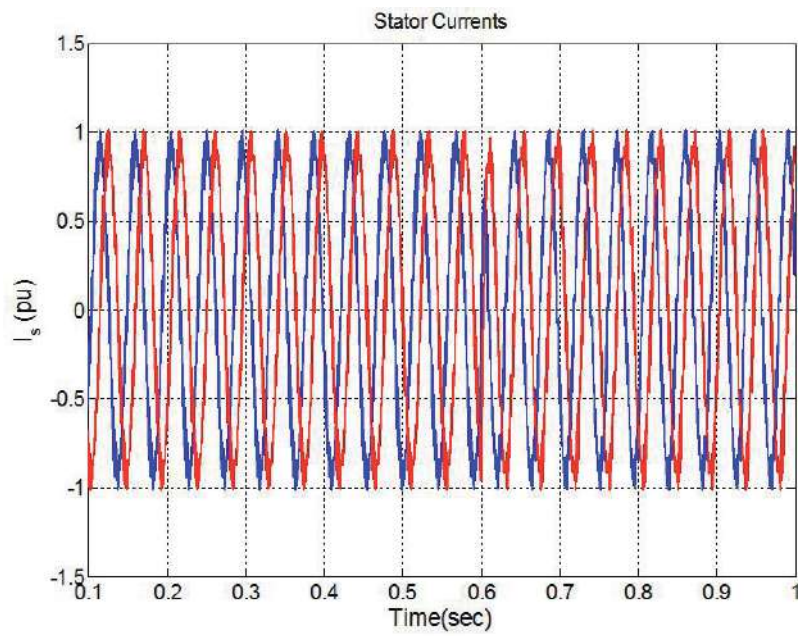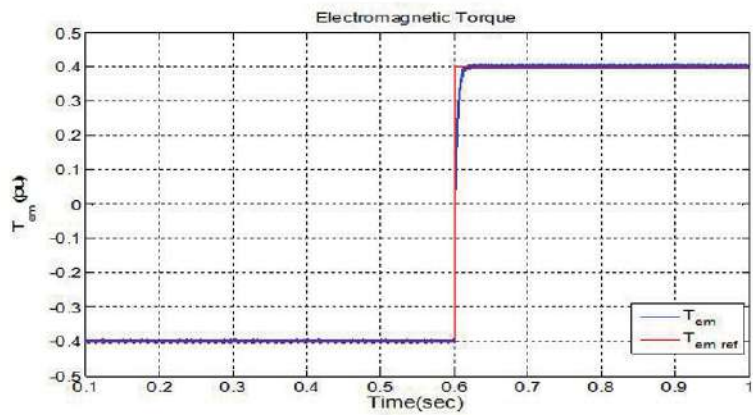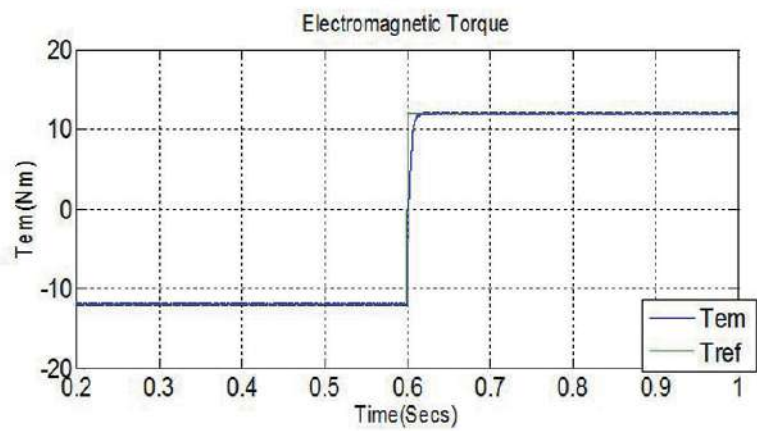
Rotor Currents

Figure 3.
(a) Response of stator currents of DFIM for step change in T_{em} from −0.4 pu to 0.4 pu at 0.6 s. (b) Torque response of DFIM for step change in T_{em} from −0.4 pu to 0.4 pu at 0.6 s, (i) proposed strategy (ii) classical DTC. (c) stator active power of DFIM for step change in T_{em} from −0.4 pu to 0.4 pu at 0.6 s. (d) Stator flux response of DFIM for step change in T_{em} from −0.4 pu to 0.4 pu at 0.6 s. (e) Response of rotor flux of DFIM for step change in T_{em} from −0.4 pu to 0.4 pu at 0.6 s. (f) Rotor speed response of DFIM for step change in T_{em} from −0.4 pu to 0.4 pu at 0.6 s. (g) Response of rotor currents of DFIM for step change in T_{em} from −0.4 pu to 0.4 pu at 0.6 s.

The torque produced by the DFIM follows as closely as the reference torque, which indicates good tracking behavior of the proposed control scheme comparative to classical DTC (not expressed in p.u. value), it can be seen in **Figure 4(b)**.

Stator flux and rotor flux responses of DFIM are shown in **Figure 4(c)** and **(d)** respectively. From the **Figure 4(c)** and **(d)**, it is observed that the variation in torque command is not having any influence on the stator and rotor fluxes of DFIM.
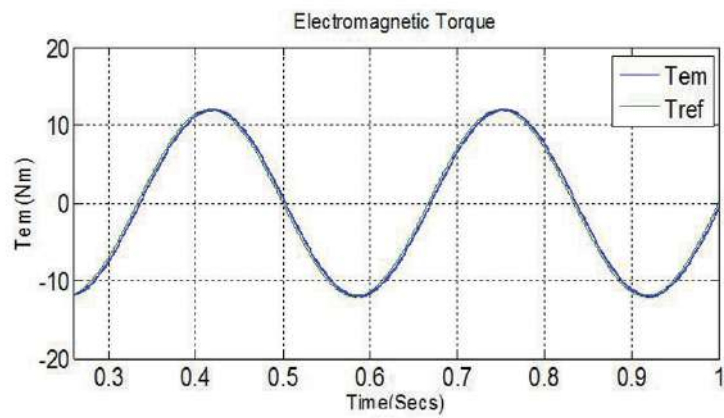
Figure 4(e) shows the rotor speed response of DFIM. From the **Figure 4(e)**, it is observed that there is continuous variation in rotor speed; of course, this variation is
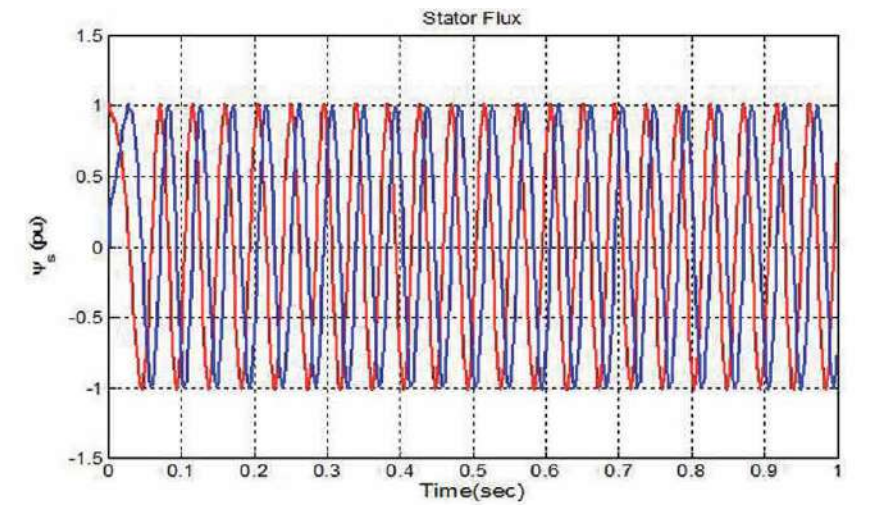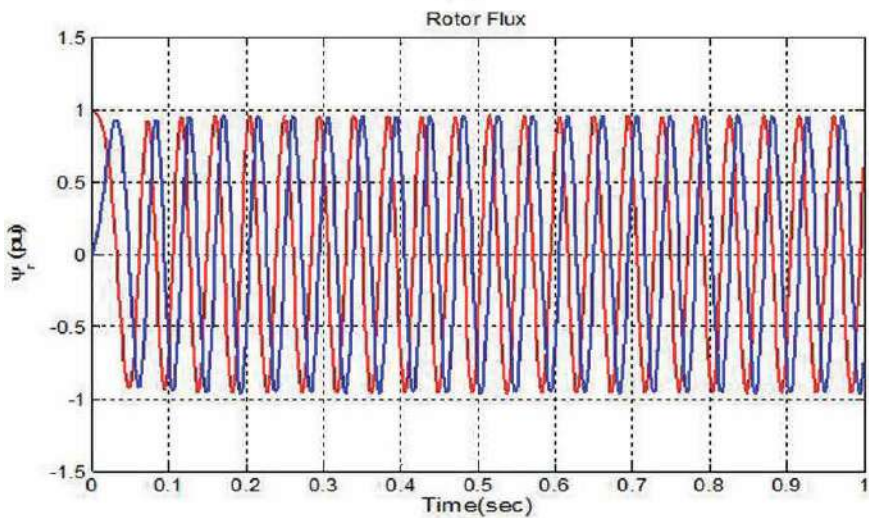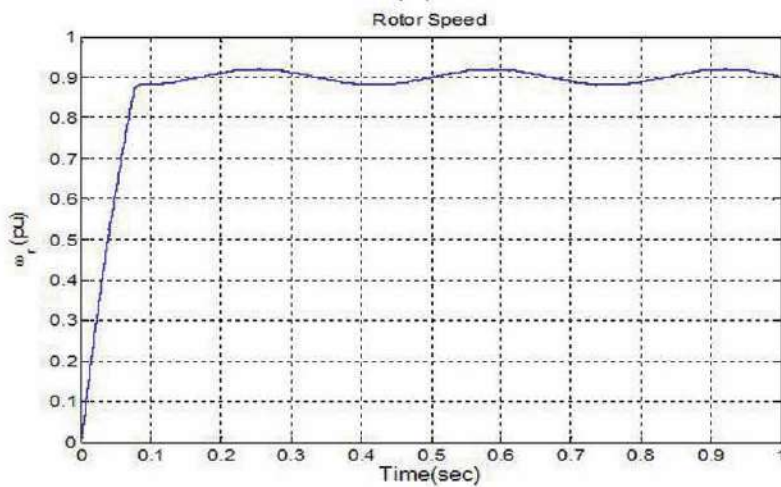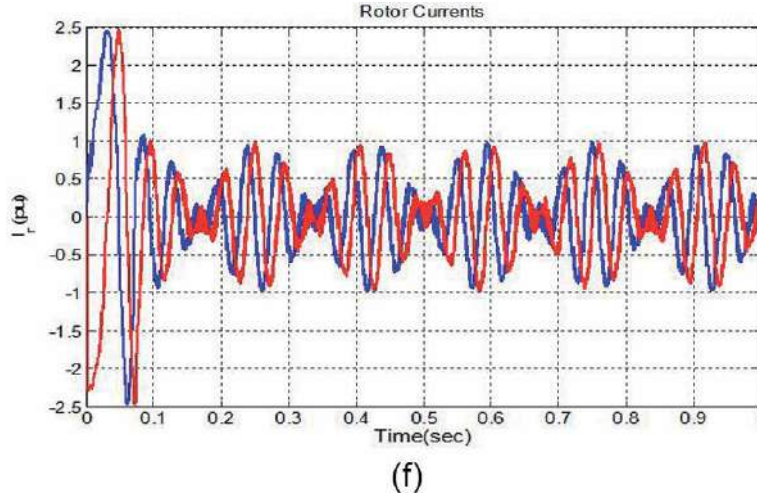
(a)

(i)

(ii)

(b)

(c)

(d)

(e)

(f)
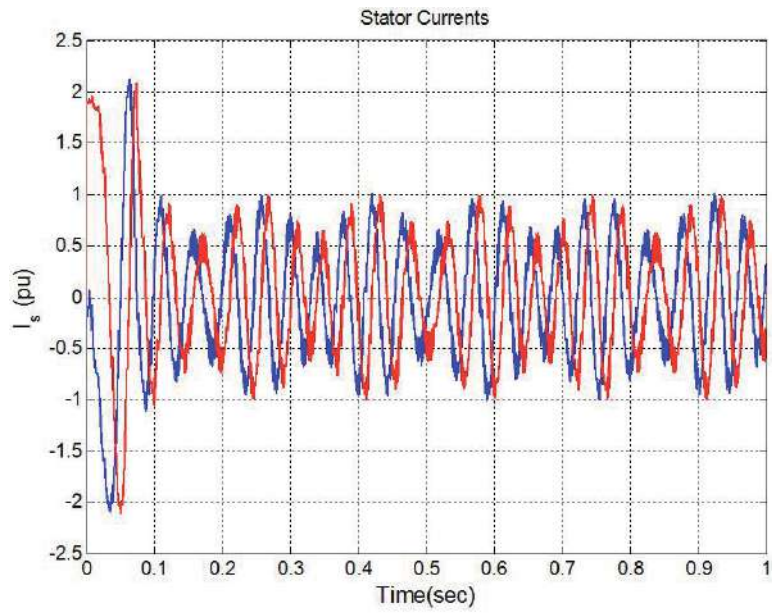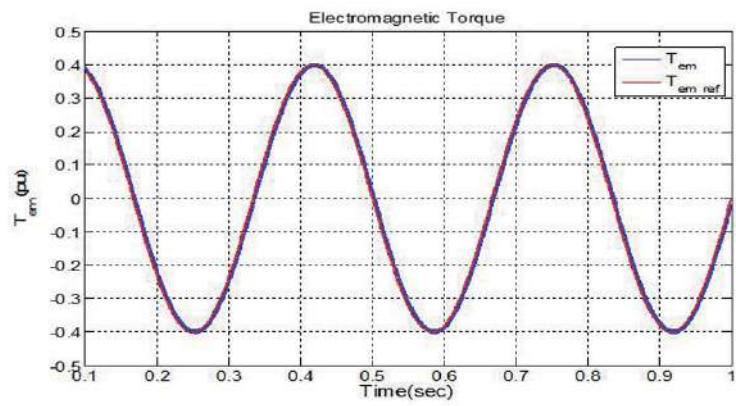
Figure 4.
(a) Response of stator currents of DFIM with variable torque command. (b) Response of developed torque of DFIM with variable torque command (i) proposed strategy (ii) classical DTC. (c) Response of stator flux of DFIM with variable torque command. (d) Response of rotor flux of DFIM with variable torque command. (e) Response of rotor speed of DFIM with variable torque command. (f) Response of rotor currents of DFIM with variable torque command.

very small it is because of variable torque command, but practically rotor speed almost constant.

The predictive DTC strategy has good tracking behavior and it is confirmed that the reduction in torque and flux ripples is achieved as there are absolute absence of over currents and reduced ripples in rotor currents as shown in **Figure 4(f)**. From the **Figure 4(f)**, it is noticed that there is continuous increase and decrease in the amplitude of rotor currents, similar to stator currents as shown in **Figure 4(a)**.

5.3 Performance of DFIM near synchronous speed

In this Section, the performance of the proposed control scheme of DFIM has been investigated near the synchronous speed. This is examined by varying the speed of DFIM from 1580 rpm (hyper synchronous value) to 1340 rpm (sub synchronous value) in terms of sine wave with frequency of 3 rads^{-1} and phase shift of 90°, with the reference values of torque and rotor flux are set to 0.4 pu and 1 pu respectively.

Even when the speed command is varied suddenly from hyper synchronous value to sub synchronous value no much transient peaks occur in stator currents, as shown in **Figure 5(a)**, which clearly emphasizes there is reduction in over currents in stator and this is because of proper selection of switching sequence of rotor voltage vectors.

As shown in **Figure 5(b)**, the torque developed by the machine for proposed strategy and classical DTC and it closely follows the reference torque which means the dynamic performance of the machine is quite satisfactory but when the rotor speed nears the synchronous speed at around 0.5 s, variable torque ripple is produced. This variability in the torque ripple is due to continuous selection of zero voltage vectors at that instant. It indicates, the smaller amplitude of rotor voltage vector is required at the instant of rotor speed nearing the synchronism, which
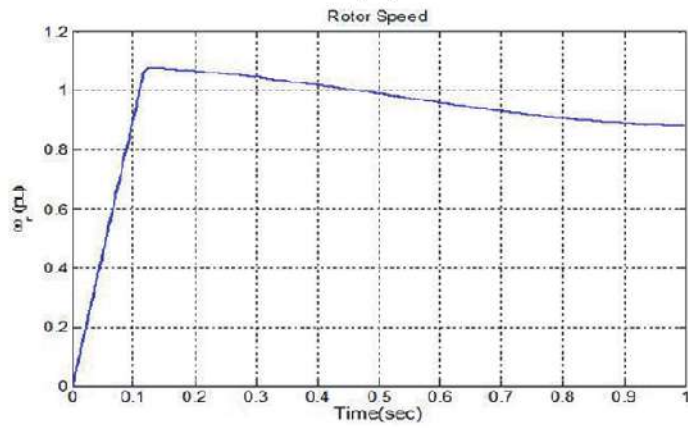
(a)

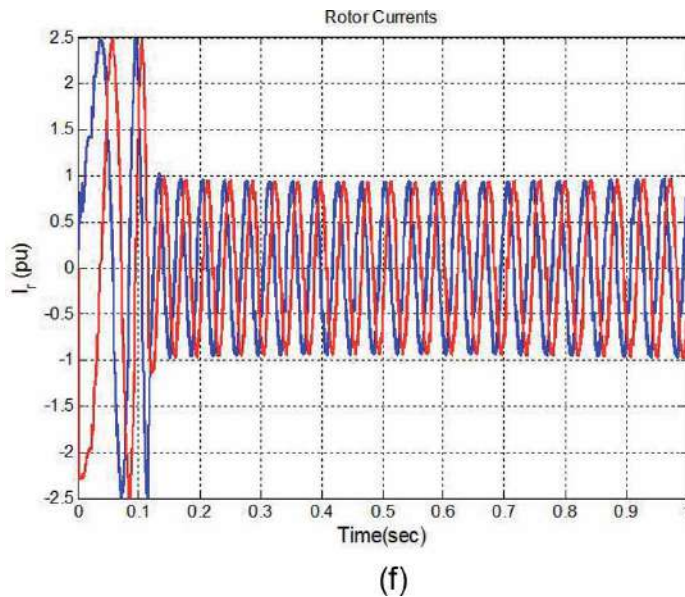

(i)

(ii)

(b)
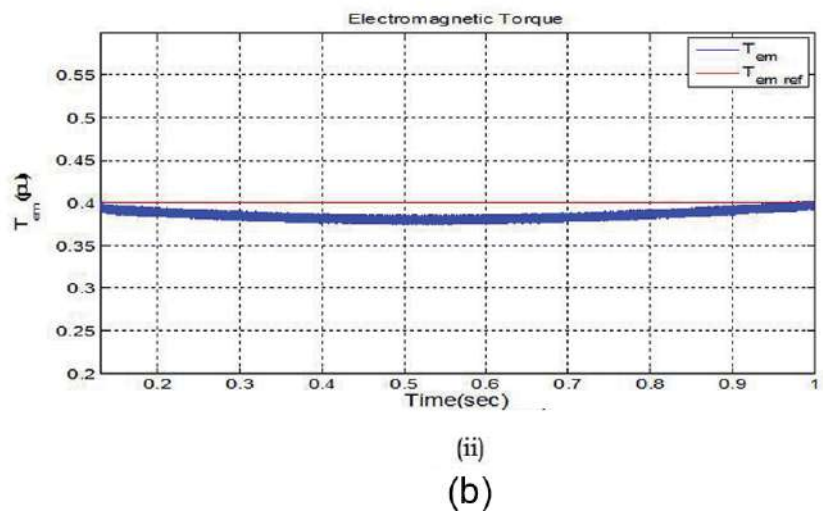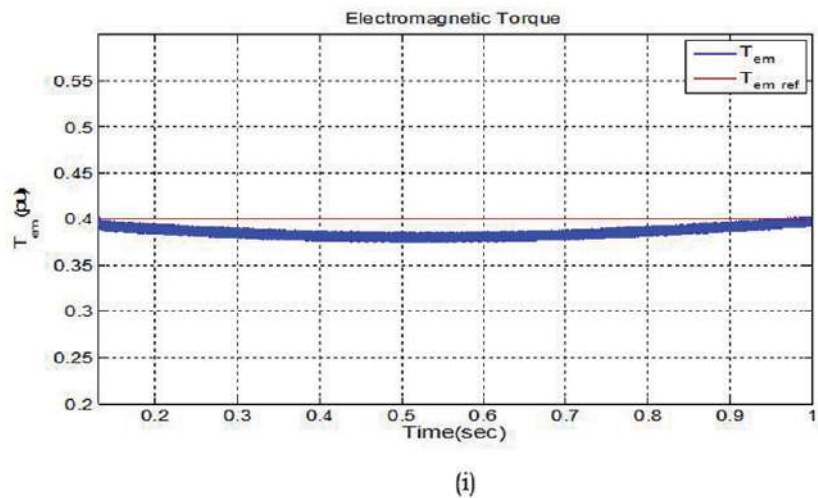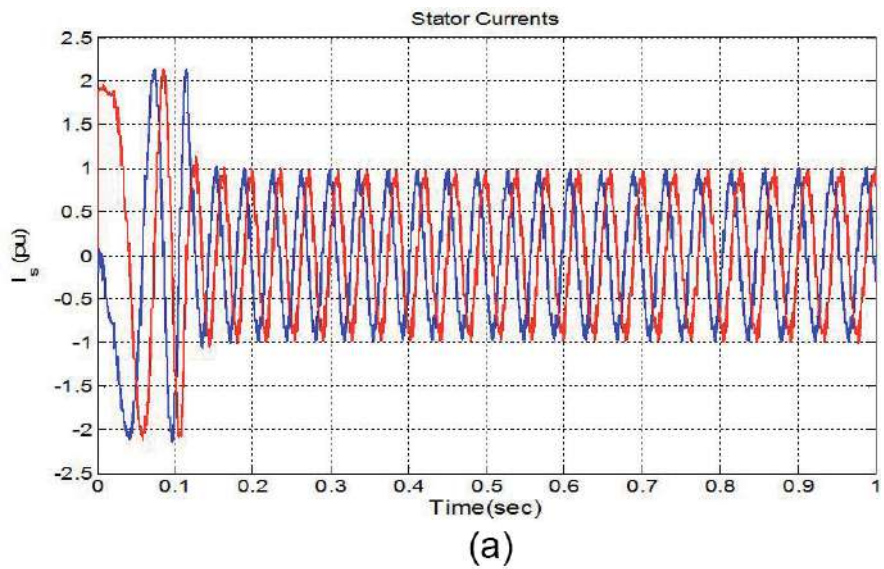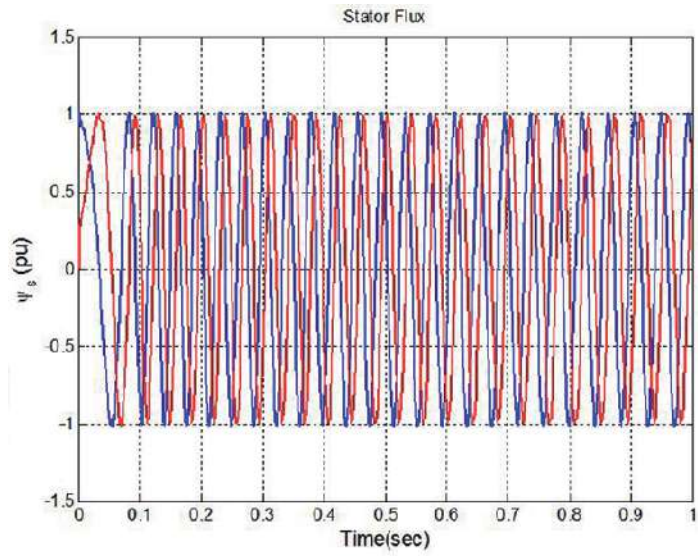
(c)
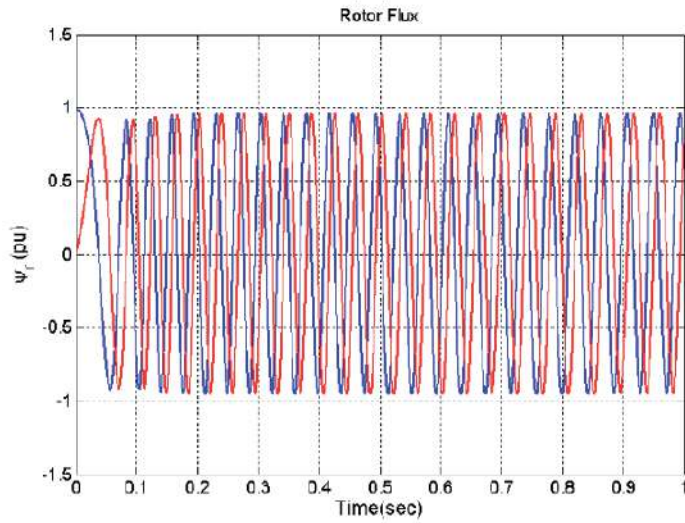
(d)

(e)

Figure 5.
(a) Response of stator currents of DFIM with variation in rotor speed from 1580 to 1340 rpm. (b) Torque response of DFIM with variation in rotor speed from 1580 to 1340 rpm (i) proposed strategy and (ii) classical DTC. (c) Response of stator flux of DFIM with variation in rotor speed from 1580 to 1340 rpm. (d) Response of rotor flux of DFIM with variation in rotor speed from 1580 to 1340 rpm. (e) Rotor speed of DFIM with variation in rotor speed from 1580 to 1340 rpm. (f) Response of rotor currents of DFIM with variation in rotor speed from 1580 to 1340 rpm.

actually causes the reduction in torque ripple and this leads to degradation of quality of control. As shown in **Figure 5(b)**, the ripples are reduced in electromagnetic torque response.

Stator flux responses are shown in **Figure 5(c)**. From the figure, it is observed that the stator flux remains constant and is not affected by change in rotor speed and also it is sinusoidal in nature.

The response of rotor flux is shown in **Figure 5(d)**, from the figure, it is observed that there is no effect on the rotor flux due to sudden change in the rotor speed and rotor flux is also not affected by the changeover.

The response of rotor speed is as shown in **Figure 5(e)**, when reference speed is varied from hyper synchronous value to sub-synchronous value and it is observed that the rotor speed response of DFIM follows the command speed.

Similar to stator currents as shown in **Figure 5(a)**, no much transient peaks occur in rotor currents, as shown in **Figure 5(f)**, that is, there is reduction in over currents in the rotor, which is because of proper selection of switching sequence of rotor voltage vectors.

6. Conclusions

The proposed control method makes two general contributions to the predictive control techniques. Firstly, it shows that using instead of two voltage vectors operating three appropriate vectors, allows operating at low constant switching frequency. Secondly, it is crucial to achieve the whole good performance of the DFIM, in terms of torque and current ripples by reducing the ripples of both directly controlled variables instead of only one.

From the proposed control method, it is possible to reduce the stress of the switching devices of the voltage source converter, in terms of low constant switching frequency behavior and switching power losses reduction, often demanded requirements in high power applications.

It presents good tracking behavior, capable of working at variable speed operation conditions, for both motoring and generating modes at sub- synchronous and hyper synchronous speeds when compared to DTC technique, making this control suitable for applications such as wind power generation.

The new DTC technique allows obtaining quick dynamic responses in respect to DTC method, with absolute absence of non-desired over currents in the machine. It ensures reduced torque and flux ripples, due to the control effect. The simulation results showed the effectiveness of the proposed method, to control the torque and the flux of the DFIM at considerably low constant switching frequency.

7. Summary

In this Chapter, new predictive DTC has been developed for DFIM. The proposed control scheme uses two voltage vectors instead of three voltage vectors and it allows operating at low constant switching frequency and reduces torque and flux ripples, and also capable of working at variable speed operating conditions for both motoring and generating modes at sub-synchronous and hyper synchronous speeds compared to classical DTC technique. The comparison of torque and flux ripple values (difference of maximum to minimum ripple value) and its reduction given by the difference of maximum value and minimum value to average value is given in the **Table 5** below.

S. No.	Parameter	Classical DTC scheme	Predictive DTC scheme
1	Torque ripple	0.3 pu	0.01 pu
2	Reduction in torque ripple	2.5%	1.25%
3	Rotor flux ripple	0.018 pu	0.01 pu
4	Reduction in rotor flux ripple	1.8%	1.05%

Table 5.
Torque and flux ripple reduction comparison.

Author details

Gopala Venu Madhav[1*] and Y.P. Obulesu[2]

1 Department of EEE, Anurag Group of Institutions, Ghatkesar, TS, India

2 School of Electrical Engineering, VIT University, Vellore, Tamilnadu, India

*Address all correspondence to: venumadhav.gopala@gmail.com

IntechOpen

References

[1] Blaschke F. A new method for the structural decoupling of a.C. induction machines. In: Proc. IFAC Conf., Dussesldorf, Germany, October 1971. 1971. pp. 1-15

[2] Takahashi I, Ohmori Y. High-performance direct torque control of an induction motor. IEEE Transactions on Industry Applications. 1989;**IA-25**(2): 257-264

[3] Depenbrock M. Direct self-control (DSC) of inverter-fed induction machine. IEEE Transactions on Power Electronics. 1988;**PE-3**(4):420-429

[4] Flach E, Hoffmann R, Mutschler P. Direct mean torque control of an induction motor. In: Proc. EPE'97 Conf. 1997. pp. 672-677

[5] Casadei D, Serra G, Tani K. Implementation of a direct control algorithm for induction motors based on discrete space vector modulation. IEEE Transactions on Power Electronics. 2000;**15**(4):769-777

[6] Kang JK, Sul SK. New direct torque control of induction motor for minimum torque ripple and constant switching frequency. IEEE Transactions on Industry Applications. 1999;**35**(5): 1076-1086

[7] Martins CA, Roboam X, Meynard TA, Carvalho AS. Switching frequency imposition and ripple reduction in DTC drives by using a multilevel converter. IEEE Transactions on Power Electronics. 2002;**17**(2): 286-297

[8] Sarasola I, Poza J, Rodríguez MA, Abad G. Predictive direct torque control of brushless doubly fed machine with reduced torque ripple at constant switching frequency. In: Proc. IEEE ISIE'07 Conf. 2007. pp. 1074-1079

[9] Aurtenechea S, Rodríguez MA, Oyarbide E, Torrealday JR. Predictive control strategy for dc/ac converters based on direct power control. IEEE Transactions on Industrial Electronics. 2007;**54**(3):1261-1271

[10] Pena R, Clare JC, Asher GM. Doubly fed induction generator using back-to-back PWM converters and its application to variable speed wind-energy generation. IEE Proceedings—Electric Power Applications. 1996;**143**: 231-241

[11] Gomez SA, Amenedo JLR. Grid synchronization of doubly fed induction generators using direct torque control. In: Proc. IEEE IECON'02 Conf. 2002. pp. 3338-3343

[12] Datta R, Ranganathan VT. Direct power control of grid-connected wound rotor induction machine without rotor position sensors. IEEE Transactions on Power Electronics. 2001;**16**(3):390-399

[13] Abad G, Rodríguez MA, Poza J. Predictive direct power control of the doubly fed induction machine with reduced power ripple at low constant switching frequency. In: Proc. IEEE ISIE'07 Conf. 2007. pp. 1119-1124

Chapter 6

Study of the Parameters of the Planner with a Screw Working Body

Juraev Tojiddin Khayrullaevich,
Norov Sobirjon Negmurodovich
and Musulmanov Furqat Shodiyevich

Abstract

This chapter examined the theoretical background of the use of a screw working body in front of the planner bucket and conducting experiments in laboratory conditions with the proposed working body. This work supports the practical solution of using a screw working particle in the current field planning. Significance of the work reducing traction resistance to soil movement up to 20% enables the tractor unit to work at higher speeds of translational motion; the latter contributes to increased productivity, improved planning quality and reduced cash costs per unit of work performed. The chapter was prepared under results of research in the Mechanics Laboratory of Bukhara Engineering Technological Institute.

Keywords: productivity of the screw working body, translational speed of the planning unit, screw pitch, screw diameter, drawing prisms

1. Introduction

Further development of agriculture in modern conditions determines the introduction of new advanced technologies and machines for their implementation.

As we know, for increase of volume agricultural products, it is need to intensification of agricultural production, one of the means of which is wide land reclamation, which provides, as one of the most important measures, the planning of the irrigated land surface. Alignment of the surface of the fields by the long-base planners is of great importance in the range of planning works, and research work to improve these planners is carried out both in Uzbekistan and abroad.

The analysis of the state of the issue showed the need to improve the quality of planning work, increase the productivity of long-base planners and increase the levelling ability of the latter [1, 2].

2. Literature review

By world and domestic farming practices, it has been proved that planning or levelling the surface of the fields is the main land reclamation measure designed

to eliminate irregularities on the field under sowing in the form of various rise and falls.

Many domestic and foreign scientific works [3–6] have been published on the need for field planning, authors of which have been examined the issue from different perspectives and pointed out the advantages of this operation. Moreover, there are many advantages, whether it is capital and operational planning or micro alignment. Experiments have established that under conditions of turbulent terrain, crop losses amount to 40% of the potential crop. Cotton grown on mounds and lowlands gives raw cotton of lower quality: fibre strength, grade, ripeness, etc. are reduced.

In areas with saline soil, a high-quality planning prevents the formation of saline spots (areas) and thereby ensures sustainable yields of all types of crops [6, 7]. Flushing saline lands without planning are ineffective.

According to Ref. [6], it was established that uniform soil moisture is achieved on the planned field, and the irrigation water consumption is significantly reduced.

In the United States, great importance is given to the planning of the surface of irrigated areas. Annually, in this country, approximately more than half of the irrigated areas are subject to planning [3, 6, 7]. Americans do not spare the cost of land planning, as this increases income from irrigated land and reduces the cost of production.

To ensure the high quality of the technological processes, including irrigation, it is necessary to pay special attention to the capital planning and the mandatory periodic implementation of the field operational planning.

3. Research methods

It is known that the magnitude and the nature of the change in the angular speed of a material particle determine the productivity and energy indicators for conveying the material with a screw [2, 8].

Let us consider the movement of a material particle of mass d_m located at point O of an inclined cylindrical screw at a distance r from the axis of the screw (**Figures 1** and **2**) and moving along the trajectory of the absolute movement AB; the axes τ, b and n are, respectively, tangent, binormal and normal to the trajectory of absolute motion [9]. The n axis is directed towards the centre of curvature and
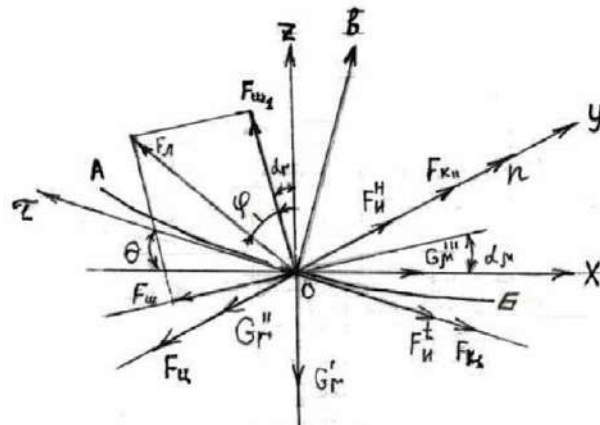

Figure 1.
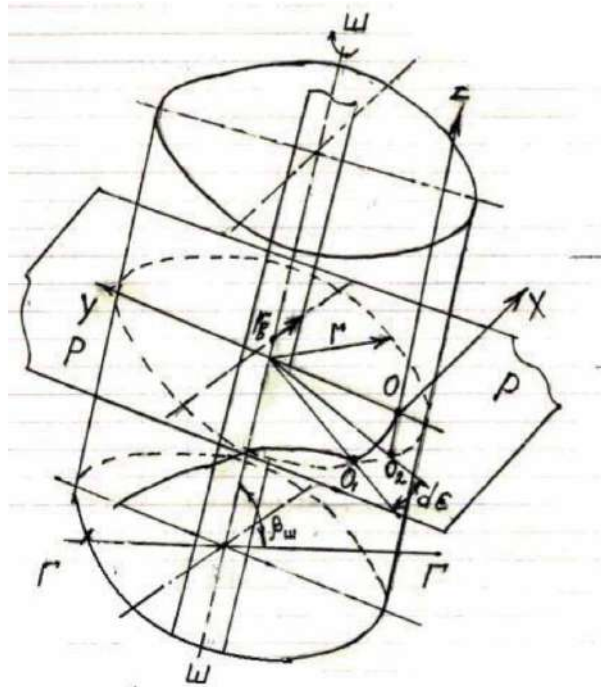*Movement of a material particle of mass d_m located at point O.*

Figure 2.
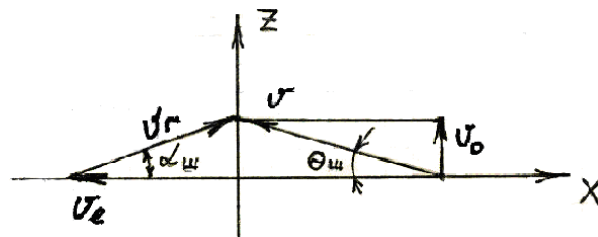*Material particle of mass d_m located at point O of an inclined cylindrical screw at a distance r.*

Figure 3.
Particle's absolute speed vector $\overline{V}$.

coincides with the y axis. The Z axis is parallel to the axis of the screw, and the x and y axes are located on tangent and normal in plane PP of the screw, perpendicular to its axis ШШШ; GG horizontal plane.

The following forces impact on the soil particle: particle gravity Gr = gdm, which can be divided into three components, axial Gr^I = Gr.sin $\beta_{ш}$ (along the z axis), radial G_r^{II} = G_r.cos $\beta_{ш}$ cosε (along the y axis) and tangent G_r^{III} = G_r.cos$\beta_{ш}$·sinε (along the x axis); centrifugal force $F_ц = \omega_r^2 \cdot \mu \cdot d \cdot m$ (along the y axis), friction force of a particle on a blade casing F_{k_1} (along the τ axis), and friction force on a helical surface $F_{ш}$ (at an angle of inclination of the helix α_r to the x axis); tangential inertial force, $F_ц{}^t$, acting along the tangent to the trajectory of the absolute motion of the particle (τ axis) and directed opposite to the particle's absolute speed vector $\overline{V}$ (**Figure 3**); normal inertial force directed to the centre of curvature of the trajectory (along the n axis); and normal reaction of the adjacent layer $F_{к_{II}}$ (along the n axis) and the helical surface $F_{ш_I}$ (at an angle a_r to the z axis). $\beta_{ш}$ is the angle of inclination of the screw to the horizon; and ε is the current angle of rotation of the particle, measured from the projection of the O_2 particle on the PP plane. The resultant $F_я$ of

the normal reaction of the helical surface F_{w_1} and the friction force against the helical surface $F_{w} = fF_{w_1}$ is deviated from the normal and the helical surface by the angle of friction $\phi = arctg f$, where f is the coefficient of friction of the soil over the screw metal. If we consider that the loosened soil before the bucket of the planner is clay, then the value of this coefficient is 0.6 ... 0.7. [8]

The friction force of a particle on a bucket caused by the combined action of forces F_{u} and G_r^{II} is equal to:

$$F_{k_1} = f_r\left(F_u + G_r^{II}\right) = f_r\left(\omega_r^2 \cdot r + g\cos\beta_{w} \cdot \cos\varepsilon\right) \cdot dm,$$

where f_r and f, respectively, are the friction coefficients of the particle on the bucket and the adjacent layer of material and the helical surface.

Absolute particle speed:

$$\vartheta = \sqrt{\vartheta_t^2 + \vartheta_o^2} = r\sqrt{\omega_r^2 + (\omega - \omega_r)^2 \cdot tg^2 a_r} \tag{1}$$

where ϑ_t is tangential particle speed at the radius r from the axis of the screw, $\vartheta_t = \omega_r \cdot r$; ϑ_o is the axial speed of the particle at a radius r from the axis of the screw, $\vartheta_o = (\omega \cdot \omega_r) tg a_r$; ω is screw angular speed; and a_r is the angle of inclination of the helix of the screw on the radius r (**Figure 2**).

The tangent force of inertia is defined as follows:

$$F_u^t = \frac{d\vartheta}{dt} dm = \frac{r[\omega_r - (\omega - \omega_r)tg^2 a_r]}{\sqrt{\omega_r^2 + (\omega - \omega_r)^2 tg^2 a_r}} \cdot \frac{d\omega_r}{dt} dm \tag{2}$$

Normal inertial force:

$$F_u^n = \vartheta^2 \cdot r_a^{-1} \cdot dm = r^2\left[\omega_r^2 + (\omega - \omega_r)^2 \cdot tg^2 a_r\right] \cdot \left[r\left(1 + tg^2\theta\right)\right]^{-1}, \tag{3}$$

where r_a is the radius of curvature of the trajectory at the selected point, $r_a = r(1 + tg^2\theta)$; and θ is the angle of inclination of the helix of the particle trajectory to the axis X (**Figure 2**)

$$tg\theta = tg a_{w}(\omega - \omega_r)\omega_r^{-1}, \tag{4}$$

where a_{w} is screw helix angle at the periphery.

According to the D'Alembert's principle [8], the equation of dynamic equilibrium of a material particle in the projections on the axis of the natural trihedral of the trajectory (τ, b, n)(**Figure 2**) will be

$$\sum\tau = \left[F_{\pi}\sin\left(a_r + \theta + \phi\right) - G_r^{III}\cos\theta - F_{k_1} - F_u^t - G_r^1\sin\theta\right] \cdot \cos\varepsilon - \\ -\left(F_u + G_r^{II} - F_u^H - F_{k^{II}}\right) \cdot \sin\varepsilon = O, \tag{5}$$

$$\sum b = \pm F_{\pi} \cdot \cos(a_r + \theta - \phi) + G_r^{III} \cdot \sin\theta - G_r^1 \cdot \cos\theta = 0, \tag{6}$$

$$\sum n = \left(F_u + G_r^{II} + F_u^H - F_{k_{ii}}\right) \cdot \cos\varepsilon + [F_{\pi}\sin\left(a_r + \theta + \phi\right) - \\ - G_r^{III} \cdot \cos\theta - F_{k1} - F_u^t - G_r^1\sin\theta] \cdot \sin\varepsilon \tag{7}$$

Solving these equations jointly, excluding the force F_{π} from them, after the corresponding transformation of the exception and time by expressing the

elementary angle of rotation along the arc O_1, O_2 (**Figure 1**) of the particle $d\varepsilon = (\omega - \omega_r)dt$, we obtain:

$$
\frac{d\omega_r}{d\varepsilon} = \pm \frac{\dfrac{sin([a_r + \phi)\omega_r + \cos{(a_r + \phi)} \cdot tga_r(\omega - \omega_r)}{\cos{(a_r + \phi)}\omega_r - \sin{(a_r + \phi)}tga_r(\omega - \omega_r)}}{(\omega - \omega_r)r[\omega_r - (\omega - \omega_r)tg^2a_r]} \rightarrow
$$

$$
\rightarrow \frac{\left[g \cdot \sin\beta_{uu} \cdot \omega_r - g \cdot \cos\beta_{uu}\sin\varepsilon \cdot tga_r(\omega - \omega_r)\right] -}{(\omega - \omega_r)r[\omega_r - (\omega - \omega_r)tg^2a_r]} \rightarrow
$$

$$
\rightarrow \frac{-f_r(\omega_r^2 + g \cdot \cos\beta_{uu} \cdot \cos\varepsilon)x\sqrt{\omega_r^2 + (\omega - \omega_r)^2 \cdot tg^2a_r} -}{(\omega - \omega_r)r[\omega_r - (\omega - \omega_r)tg^2a_r]} \rightarrow
\tag{8}
$$

$$
\rightarrow \frac{-g \cdot \sin\beta_{uu} \cdot tga_r(\omega - \omega_r) - g \cdot \cos\beta_{uu}\sin\varepsilon \cdot \omega_r}{(\omega - \omega_r)r[\omega_r - (\omega - \omega_r)tg^2a_r]}
$$

By integrating Eq. (8) by the Euler method [3], we can obtain the curves of the dependence of ω_r on ε for screws with different parameters.

In the inclined screw, there is a periodically steady motion of the material particle. The maximum value of ω_r^{max} is on the plot with the values of the angle $2k\pi > \varepsilon > (2k - 1)\pi$, and the value of ω_r^{min} is in the zone $(2k + 1)\pi > \varepsilon > 2k\pi$, where (k) is any number. In order to simplification for inclined screws, it is possible to take the average value of the angular speed in the area of periodically steady motion:

$$
\omega_r^{cp} = \int_{\varepsilon=2k\pi}^{\varepsilon=(2k+1)\pi} \cdot \omega_r d\varepsilon \cong \frac{\omega_r^{2k\pi} + \omega_r^{(2k+1)\pi}}{2}
\tag{9}
$$

The values of ω_r^{max} and ω_r^{min} can be found by progressive approximation from Eq. (8), equating the right side to zero at $\varepsilon = 2k\pi$ and $\varepsilon = (2k + 1)\pi$. However, for practical purposes, the angular speed of a soil particle at the periphery of the screw can be taken as:

for vertical screws, $0,4\omega < \omega_{r_{uu}} < 0,5\omega$,

for steeply inclined screws, $(\beta_{uu} \geq 30^o)\ 0,3\omega < \omega_{r_{uu}} < 0,4\omega$,

where $\omega_{r_{uu}}$ is the particle angular speed at the periphery of the screw, sec^{-1}.

The study of Eq. (8) showed that in a certain zone limited by the cylindrical contour of the soil shaft, soil particles relatively quickly acquire the angular speed of the screw and their lifting stops [8]. The value of the so-called critical radius $r_{\kappa p}$ depends on the initial conditions and is determined from Eq. (8) after substituting $\omega_r = \omega$ at $d\omega_r/d\varepsilon = 0$.

In the horizontal ($\beta_{uu} < 30°$) screw, during the period of steady motion, the angular speed of the particle is zero. The angle of rotation of the particle ε, at which the steady motion begins, depends on the initial conditions and can be found from Eq. (8):

$$
\varepsilon = arctg\left[f_r \sin{(a_r + \phi)} \cos^{-1}{(a_r + \phi)}\right]
\tag{10}
$$

Maximum productivity on loosened soil, determined by the throughput between the upper turns of the screw will be:

$$\Pi = \int_{r_{\kappa p}}^{r_{uu}} \vartheta_r dS, \qquad (11)$$

where r_{uu} is the outer radius of the screw; ϑ_r is the ground sliding speed on the helical surface of the screw (relative speed); and dS is the elementary cross-sectional area of the soil located between the upper turns in a plane perpendicular to the relative speed vector.

The screw capacity in a dense body will be:

$$\Pi_T = \frac{1}{K_p} \int_{\kappa_{\kappa p}}^{r_{uu}} \vartheta_r \cdot dS^I, \qquad (12)$$

where κ_p is soil loosening coefficient; for our case, $\kappa_p = 1.14 \ldots 1.28$ [8].

Soil in the cross section of the screw by a plane, passing through the axis of the screw, occupies an area bounded from below by a straight-line perpendicular to the axis of the screw (**Figure 4**). Then in the cross section, we get a rectangle of length l^{II}, which can be taken equal to the pitch of the screw $l^{II} = l^I_{uu}$.

The elementary area of soil cross-section at a distance r from the screw axis will be equal to:

$$dS = dS_1 \cdot \cos a_r = l^1{}_{uu}d_r \cos a_r = 2\pi l^1{}_{uu}\left(\sqrt{4\pi^2 \cdot r^2 + \left(l^1{}_{uu}\right)^2}\right)^{-1} \cdot rd_r, \qquad (13)$$

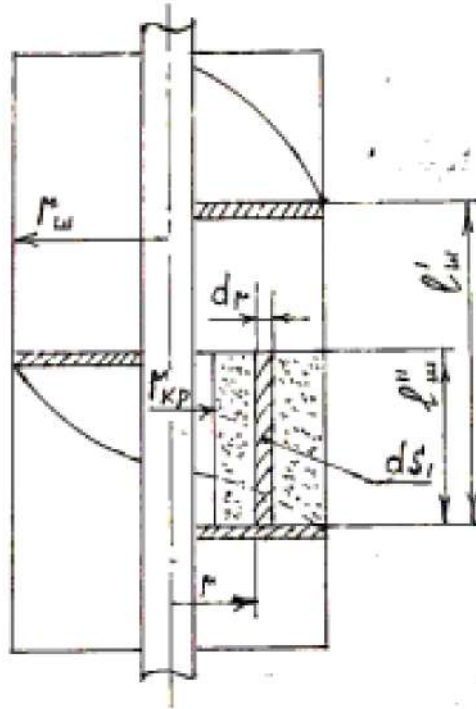where dS_1 is the elementary area of soil in axial cross-section (**Figure 4**).

Figure 4.
Position of soil area in the cross section of the screw.

In horizontal and gently dipping screws at inclination angle $\beta_{ш} \leq 30°$, the angular speed of the material particle is $\omega^{cp}{}_{r_{ш}} = 0$. To calculate the capacity (m³/h), we can use [1] the following formula:

$$\Pi_T = 450\left(d_{ш}{}^2 - d_b{}^2\right)l_{ш}{}^1\omega \cdot K_H K_\beta \cdot K_p{}^{-1}, \qquad (14)$$

where $d_{ш}$, $d_в$, respectively, are the diameters of the screw and shaft, m; $K_н$ is the screw filling coefficient, for our case we can take equal to $K_н = 0,2 \ldots 0,4$; and K_β is the coefficient taking into account the angle of inclination of the screw to the horizon $\beta_{ш}$, $K_\beta = 1,0 \ldots 0,8$ [8].

3.1 Selection and justification of the main parameters of the screw

The main parameters of working elements of the screw include the length of the conveying part—$l_{ш}$, the length of the cutting part—l_p, the diameter of the screw—$d_{ш}$, peripheral speed on the cutting edge—$\vartheta_{окр}$, the pitch of the screw—$l^1{}_{ш}$ and the working speed of movement—ϑ_p.

The length of the conveying and cutting parts of the screw is taken constructively, based on the type of screw and the parameters of the medium being processed. For preliminary calculations, we can take the length of the conveying part of the horizontally located screw $l_{ш} = l_p = (0,7 \ldots 0,8)\, в_n$, where $в_н$ is the width of the planner scoop.

The diameter of the screw $d_{ш}$ with a horizontal working body at the given productivity $\Pi_г{}^1 = \Pi_т$ can be determined from formula (14) after some transformations, m;

$$d_{ш} \geq \sqrt{\Pi_T{}^1 \cdot K_p\left(900\vartheta_{окр} \cdot K_a K_н \cdot K_\beta\right)^{-1} + d^2{}_в}, \qquad (15)$$

where $\vartheta_{окр}$ is the peripheral speed on the cutting edge of the screw, $\vartheta_{окр} = 1.5 \ldots 3$ m/sec; and K_a is the coefficient taking into account the inclination of the cutting edge of the screw, $K_a = l^1{}_{ш}/d_{ш} = 0,7 \ldots 1,0$. Other designations see from the formula (14).

The step of the horizontal screw $l^1{}_{ш}$ is taken equal to $l^1{}_{ш} = K_a d_{ш}$, the value of K_a is taken depending on the inclination of the cutting edge of the screw. For our case, we can take K_a equal to 0.85.

The working speed of the soil movement with the screw should be equal to the speed of filling the planner bucket with soil. The latter depends on the forward speed of movement of the planner. For our case, with a certain accuracy, we can take $\vartheta_{гр} = \vartheta_{ков} = \vartheta_п$, where $\vartheta_{гр}$ is the speed of the soil movement with the screw, $\vartheta_{ков}$ is the speed of filling the planner bucket with soil and $\vartheta_п$ is the forward speed of the planner, m/s.

The working speed of the planner's movement can also be determined from the conditions for ensuring a given efficiency on a cut of soil with the planner's bucket. For a horizontal screw, operating speed ($\vartheta_п$) of movement is (m/s):

$$\vartheta_\Pi = \Pi_T \cdot l_p{}^{-1} \cdot h_p{}^{-1}, \qquad (16)$$

where $\Pi_г$ is the efficiency of the planning unit on cut of soil, m³/sec; $l_р$ is the cutting length of the planner's knife, m; and $h_р$ is the thickness of the cut soil layer, m.

Based on the analysis of the above theoretical background in the determination of the efficiency of the screw working body, it is suggested that with the increase in

the speed of rotation and in diameters of the screw, the productivity of the screw working body increases. The screw pitch is also of great importance, with an increase in which the volume of soil moved to the sidewalls of the planner bucket increases, which in turn contributes to an even distribution of the soil of the drawing prism along the width of the planner passage. With an increase in the speed of forward movement of the planner increases the working capacity of the screw working body, that is screws move a large volume of soil to the sides relative to each other. However, such an improvement in the work of working element of the screw for our case, as shown by selective experiments with the experimental sample of a mini-planner, occurs up to a speed of 2 m/s of the forward movement of the unit. Above this speed, the screws begin to become clogged with soil, and the technological process of the screw working body is violated.

We derived the equation of traction resistance of the planner, which has the following form:

$$P = f_n G_n + \frac{\left[\sin\beta(1 - f^2)2f\cos\beta\right]\tau \cdot S}{\sin(\beta + \theta)(1 - \mu f) + \cos(\beta + \theta)(\mu + f)} + \frac{1}{3}\lambda_v l^3 tg^2\varphi_0 tg^2\left(45 - \frac{\beta}{2}\right)f +$$

$$+ G_{np}\left(f\cos^2\beta + tg\rho + \frac{2V^2\sin^2\frac{\beta}{2}}{Kycm \cdot g} \right)$$

(17)

where f_n- planner rolling resistance coefficient; G_n- mass of the planner; $\beta-$ cutting angle; $f, \mu-$ coefficients of friction of soil on steel and soil on soil; $\tau-$ shear stress; $S-$ shear area; $\theta-$ shear angle; λ_v- volumetric mass of soil as in the function of movement speed; $l-$ bucket side length; φ_0- angle of slope of the soil roller during movement; $G_{np}-$ mass of the soil roller; $V-$ unit movement speed; and $Kycm-$ coefficient taking into account the design of the rear wall of the bucket [10].

4. Results and discussion

From the analysis and conclusions we can see that with the increase in the rotation speed and diameter of the screw, the productivity of the screw working element increases. The screw pitch is also of great importance, with an increase in which increases the amount of soil movement to the sidewalls of the planner bucket, which in turn contributes to uniform distribution of the soil of the drawing prism along the width of the planner. With the increase in the speed of translational movement of the planner increases the functionality of the screw working element, that is the screws move a large volume of soil to the sides relative to each other. Below in **Figure 5**, the location of the screws in the bucket of the planner is shown.

However, such improvement in the work of the screw working element for our case, as shown by selective experiments with the experimental sample of a mini-planner, occurs up to the speed of 2 m/s of translational movement of the unit. Above this speed, the screws begin to be clogged with soil, and the technological process of the screw working body is violated. Below in **Figure 6**, experimental sample of a mini-planner with a screw working body is shown.

The above analysis requires investigating the productivity of the screw working body, depending on the rotation speed, diameter and pitch of the screw. Therein, the translational speed of the planning unit is also of significant importance. Because, the volume of the planner's bucket filled with soil per unit of time should be equal to the volume of the processed soil by the screws.
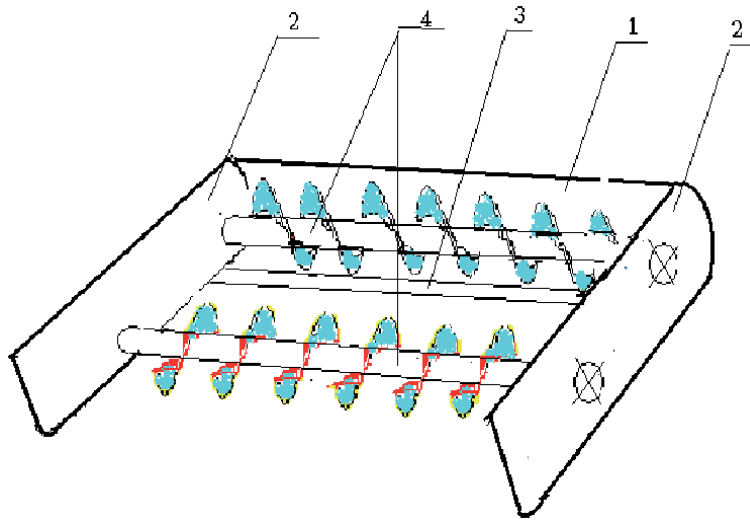
Figure 5.
Scheme of the location of the screws in the bucket of the planner (1—rear wall of the bucket, 2—tank walls, 3—knife of the rear wall and 4—screws).

Figure 6.
General view of the experimental prototype of the mini planner.

Below are the curves (**Figures 7–9**) of the change in productivity of the screw working element of the planner depending on the rotation speed, diameter and pitch of the screw.

As we can see from the graph (**Figure 7**), with the increase in screw rotation, the screw productivity is directly proportional to screw rotation. At a screw rotation of 40 rpm, the screw capacity is 2.56 m^3/h, and at screw rotation of 240 rpm, the screw capacity increases to 15.38 m^3/h. That is, the productivity of the screw increases by six times. This increase in productivity approximately corresponds to the desired performance of the planning unit.

The change in the performance of the screw in the function (D_s) of the diameter of the screw is shown in **Figure 8**.

Analysing this graph, we can say that the change in productivity along its diameter has curvilinear nature. Moreover, part of the curve to the point corresponding to D_s = 180 mm is a power-law nature, and then the curve changes linearly. Further increase in the diameter of the screw (D_s) leads to the increase in its productivity so that the planner will not be able to provide the screws with soil for their normal operation. In addition, the increase in the given productivity of the
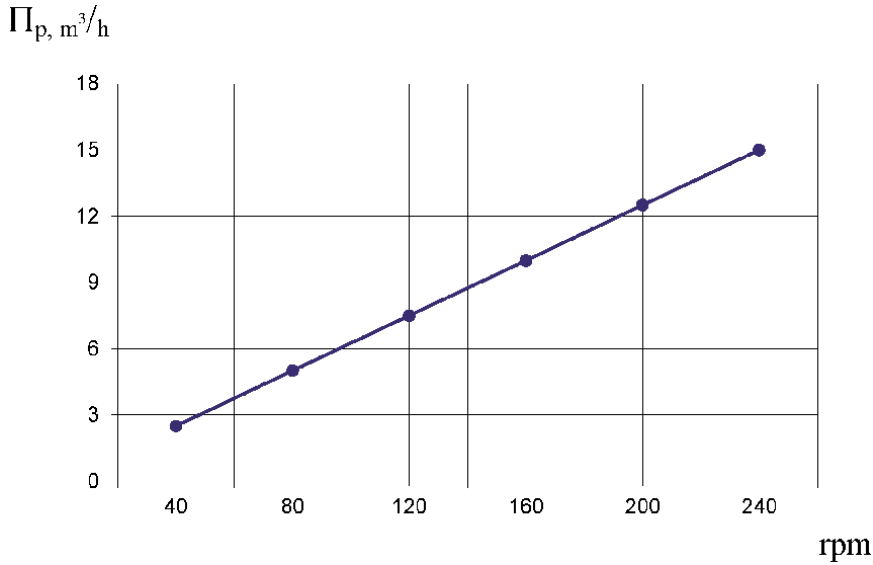
Π_{p}, m³/h

Figure 7.
Change of the productivity of the screw working element depending on the speed of rotation of the screws (at D_p = 0.18 m, S_p = 0.15 m and $K_н$ = 0.28—bucket filling ratio).

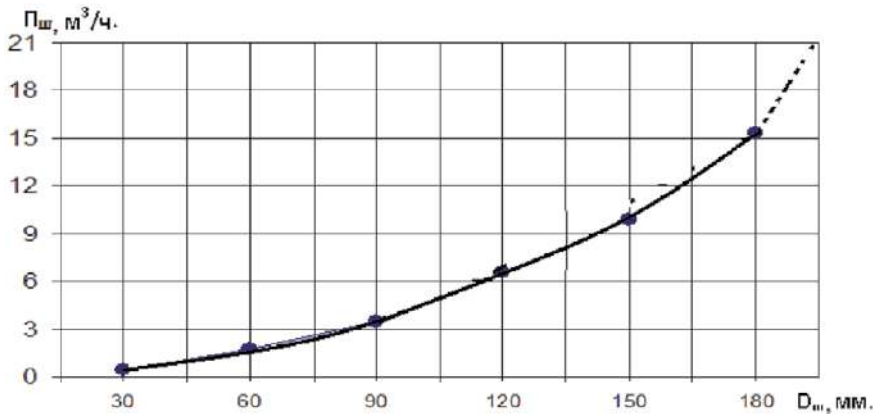**Figure 8.**
Change in productivity of the screw working element depending on the diameter (Ds) of the screw (at S_s = 0.15 m, n_s = 240 rpm and $K_н$ = 0.28).

scheduler, which is accompanied by the increase in the translational speed of the movement of the unit above 7.5 km/h, leads to a disruption of the technological process of planning and the decrease in the quality indicators of field levelness [3].

The graph of the performance of the screw working element depending on the pitch (S_m) of the screw is shown in **Figure 9**.

As we can see from the graph, with the increase in the pitch of the screw (S_s), its productivity changes in direct proportion to the changes in the pitch (S_s), that is the functional change in the curve is linear. If with a screw pitch of 30 mm, the screw capacity is 3.07 m³/h, then with a screw pitch of 180 mm, the productivity increases to 18.45 m³/h, that is it increases six times.

Analysis of the graph (**Figure 9**) shows that increasing the screw pitch to 180 mm increases the capacity to 18.45 m³/h, which is almost to 3 m³ more than at the screw pitch S_s = 150 mm. Such an increase in the productivity of the screw
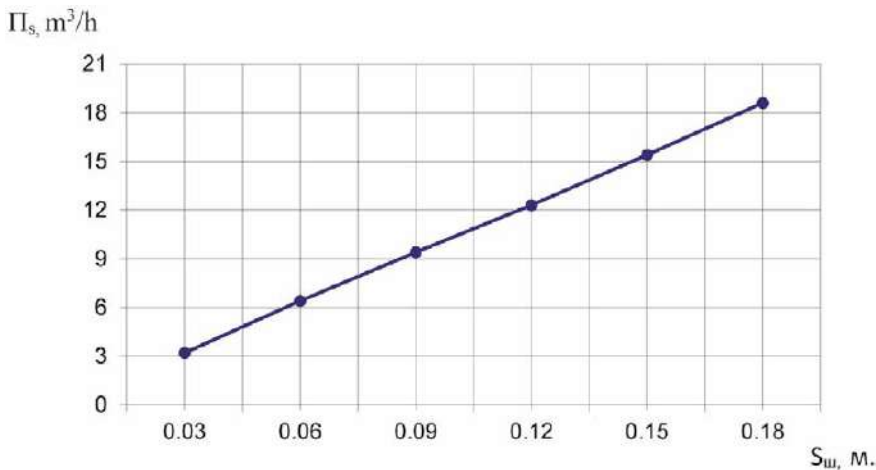
$\Pi_s,\ m^3/h$

Figure 9.
Change in the productivity of the screw working element depending on the pitch (S_s) of the screw (at $D_s = 0.18\ m$, $n_s = 240\ rpm$ and $K_\text{н} = 0.28$).

working element could be obtained with a further increase in its diameter (D_s). But it is known that the increase in the diameter (D_s) of the screw is accompanied by greater energy consumption during its operation compared to the increase in the pitch of the screw. Therefore, a theoretical study of the work of the screw working element in the bucket of the planner allows us to conclude that for a given productivity of the planning unit, it is advantageous and advisable to use the screw parameters: D_s = 180 mm, n_s = 240 rpm and screw pitch S_s = 180 mm.

Increase in the productivity of the screw working element due to the increase in the pitch of the screw reduces the metal consumption of the screw and the corresponding material costs in comparison with the increase in the diameter (D_s) of the screw. In addition, further increase in the diameter of the screw causes difficulties in their layout in the bucket of the planner.

Using the methodology for conducting scientific research and processing the obtained data [2, 10], we derived empirical equations (formulas) of dependencies $y = f(n_\text{ш})$, $y = f(D_\text{ш})$ and $y = f(S_\text{ш})$. For the graphs of **Figures 7–9**, respectively, $y_1 = 0,064X$; $y_2 = 474,7X^2$; and $y_3 = 102,5X$, the curve of which is consistent with the curves shown in **Figures 7–9**.

The screw working body surface was geometrically modelled by corresponding author and the offered geometric models give possibility to control engineering and technological parameters by optimization of geometric parameters of working surface, which may use this possibility in designing the working body of screw planners through exporting CAD models to CAE system [9, 11–15].

Author details

Juraev Tojiddin Khayrullaevich[1]*, Norov Sobirjon Negmurodovich[2]
and Musulmanov Furqat Shodiyevich[1]

1 Tashkent Institute of Irrigation and Agriculture Mechanization Engineers,
Bukhara Branch, Uzbekistan

2 Bukhara Engineering-Technological Institute, Uzbekistan

*Address all correspondence to: tojiddin_1968@mail.ru

IntechOpen

References

[1] Khasanov IS, Norov SN. Theoretical background of the results of experiments on the use of screw before the planner bucket. Universum: Technical Sciences Moscow. 2019;**12** (69):41–44

[2] Norov SN, Hamraeva MF. Analytical research of determining the maximum efficiency of planning machines. International Journal of Advanced Research in Science, Engineering and Technology. 2019;**6**(6):361-362. Available from: http://www.ijarset.com/upload/2019/june/37-IJARSET-Abrorov-51.pdf

[3] Norov SN. Research and Development of a Machine System for Complex Mechanization of Precultival Treatment of Agricultural Conditions in the Bukhara Region. Deutschland, Germany: LAP LAMBERT Academic Publishing; 2019. p. 65. Available from: https://www.lap-publishing.com/

[4] Efremov AN. Laser Planning of Irrigated Lands. Moscow. 2016. Available from: https://www.ya-fermer. ru/sites/default/files/lasernayapla nirovka_0.pdf

[5] Antonov EV. Development of technological process of planning rice drafts using the multifunctional planning machine [Dissertation for the degree of candidate of technical sciences]. Russia. 2008

[6] Efremov AN, Yu NS. Machines and technologies of capital planning of rice drafts. Tractors and Agricultural Machinery. 2016;**3**:37

[7] Efremov AN. The method of calculating the operational efficiency of levers. Construction and Road Machines. 2015;5:42-46

[8] Khasanov IS, Norov SN. Theoretical background for determining some parameters of the screw working jointly with the planner bucket. Agrarian Science Journal, Moscow, 2015;**6**

[9] Juraev TK. Design the working surface based on the particle trajectory. In: Proceeding Outs of Conference "AVIA-2013". Kiev: NAU; 2013. pp. 21–23. Available from: https://scholar.goog le.com/scholar?cluster= 79868844450713291378&hl=en&oi=sch olarr

[10] Norov SN. Theoretical background for research of tractive effort of the planner. In: Collected papers of XXII International Scientific-Practical conference "Russian Science in the Modern World". Moscow. 2019. Available from: http://xn–80aa3afkg vdfe5he.xn–p1ai/RNSM-22_originalma ket_N-1.pdf

[11] Juraev TK. Decision maintenance management problems in agriculture Engineering by Constructive Geometric Modeling Methods. Maintenance Management. Edited by Fausto Pedro García Márquez and Mayorkinos Papaelias. London, United Kingdom. 2020. pp. 23-37. https://mts.intechopen. com/storage/books/8623/authors_book/.

[12] Juraev T.Kh, Murodov N.M, Naimov S.T. Application the Geometric Modeling Methods and Systems in Design Engineering and Manufacturing on Example of Agriculture Engineering. /Design and Manufacturing. /Edited by Evren Yasa, Mohsen Mhadhbi and Eleonora Santecchia. First published in London, United Kingdom, 2020 by IntechOpen, 211-231 p. http://dx.doi. org/10.5772/intechopen.83290.

[13] Juraev TK. Creating the geometric database for product lifecycle management system in agricultural engineering. In: International Conference on Information Science and Communications Technologies ICISCT

2017 Applications, Trends and Opportunities; 2-4 November 2017, TUIT, Tashkent, Uzbekistan. IEEE Catalog Part Number: CFP17H74-CDR, ISBN: 978-1-5386-2167-7. 2017. Available from: https://www.researchga te.net/publication/321821311

[14] Juraev TK. Conceptual design of moldboard based on geometric modeling. In: Theory and Application of Design. Kiev: NAU; 2012. №. 1. pp. 75-81. Available from: http:// www.irbis-nbuv.gov.ua/cgi-bin/irbis_ nbuv/cgiirbis_64.exe?C21COM=2& I21DBN=UJRN&P21DBN=UJRN& IMAGE_FILE_DOWNLOAD=1& Image_file_name=PDF/tprd_2012_1_13. pdf

[15] Juraev TK. Modeling the directory curve of moldboard surface by conic. Applied Geometry and Engineering Graphic. Kiev: KNUCA; 2011. №. 87. Available from: https://scholar.google. com/scholar?cluster= 2210113268218384828&hl=en&oi= scholarr

Chapter 7

Torque Ripple Reduction in DTC Induction Motor Drive

Adhavan Balashanmugham, Maheswaran Mockaisamy and Sathiyanathan Murugesan

Abstract

The asynchronous or Induction Motor (IM) is one of the most widely used electrical machines in the world, due to the three following advantages namely 1. Their construction is simple and rugged 2.The absence of slip rings, commutators and brushes make it cheaper, and 3.It is also maintenance free compared to DC motors and Synchronous motor due to wear and tear of brushes, slip rings and commutators respectively. The Section 1 deals with the introduction of induction motor and Direct Torque Control scheme. Section 2 briefly discusses the types of Induction motor. Section 3 tells about the control strategies of Induction motor respectively scalar control and vector control, and also briefly explains about Direct Torque Control (DTC) method. The Section 4 discuss about the Types of Control Strategies for Torque ripple Reductions in DTC as well as the two proposed schemes namely 1.Fuzzy Logic Controller (FLC) for DTC-SVM and 2.Artificial Neural Network (ANN) controller for DTC-SVM respectively for IM and its results, The two proposed schemes uses Hybrid Asymmetric Space Vector Pulse Width Modulation (HASVPWM) for switching the inverter. The Section 5 revels about the modern advanced techniques such as ANN and FLC based DTC.

Keywords: types of IM, control techniques of IM, direct torque and flux control (DTC), torque ripple reductions in DTC, modern strategies of DTC, fuzzy logic controller (FLC) for DTC-SVM, artificial neural network (ANN) controller for DTC-SVM, hybrid asymmetric space vector pulse width modulation (HASVPWM)

1. Introduction

The electric motors are electromechanical machines, which are used for the conversion of electrical energy into mechanical energy. The foremost categories of AC motors are asynchronous and synchronous motors. The asynchronous motors are called singly excited machines, that is, the stator windings are connected to AC supply whereas the rotor has no connection from the stator or to any other source of supply. The power is transferred from the stator to the rotor only by mutual induction, owing to which the asynchronous motors are called as induction machines. The induction motor is used widely in several industrial applications because of the following advantages 1. Ruggedness 2. Good efficiency 3. Simple and easy control. When the induction motor is compared to separately excited DC drives it is inferior because of coupled torque and flux. To bring high performance in induction motor drive the advanced control techniques of induction motor uses independent control of torque and flux, like in separately excited DC drives.

The advanced control techniques such as field oriented control and direct torque control play vital role in today's high performance AC drives. Later in the 1980s, the direct torque control (DTC) method was proposed by Takahashi and Depenbrock [1, 2]. The direct torque control is a robust method compared to other methods. In this method by selecting optimum inverter switching modes the motor torque and flux are controlled independently and also direct. The primary input of the motor is stator voltage and stator current. From this the stator flux and electromagnetic torques are calculated. The torque errors and flux errors are limited within the hysteresis band. The Direct torque control of induction motors based on discrete space vector modulation using adaptive sliding mode control was proposed by Ben Salem and Derbel [3], the results shows the effectiveness and the robustness of the DTC- discrete SVM adaptive sliding mode control of induction motors. The variations of induction motor parameters is shown by Ben Salem and Derbel in their subsequent two publications namely Performance Analysis of DTC-SVM Sliding Mode Controllers-Based on Estimator of Electric Motor Speed Drive [4], and DTC-SVM Based Sliding Mode Controllers with Load Torque Estimators for Induction Motor Drives [5] respectively. The advantages of this direct torque control method is improved efficiency and fast response of torque in dynamic conditions [6, 7].

2. Types of induction motor

A typical three phase Induction motor consists of two parts namely stator and rotor, the outer part is called stator having coils supplied with three phase AC current to produce a rotating magnetic field. The inside rotating part is called rotor attached to the output shaft that is gives the useful torque produced by the rotating magnetic field. The stator is made up of stack of steel laminations of 0.35-o.5 mm thick with slots similar to a stator of a synchronous machine. The Coils are placed in the slots to form a three or single phase winding. **Figure 1A** shows the stator stampings with slots of induction motor **Figure 1B** shows the stator of induction motor [6].

The rotors of induction motors are of two types namely squirrel cage rotor and slip ring rotor. The squirrel cage rotor is made up of punched laminations with (0.35 to 0.5) mm thick steel core with rotor slots. Aluminum bars are molded in the slots instead of winding. End rings short circuit the aluminum bars at each side [6]. **Figure 2** shows the squirrel cage rotor.

The slip ring rotor or wound rotor has windings like the stator and at the end of each phase the winding is connected to a slip ring. There are three slip rings and

Figure 1.
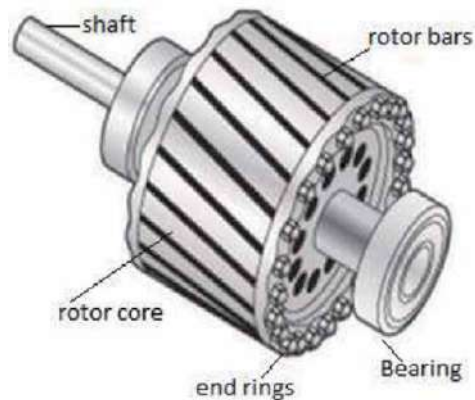*(A) Stator stamping with slots of induction motor. (B) Stator of Induction Motor.*
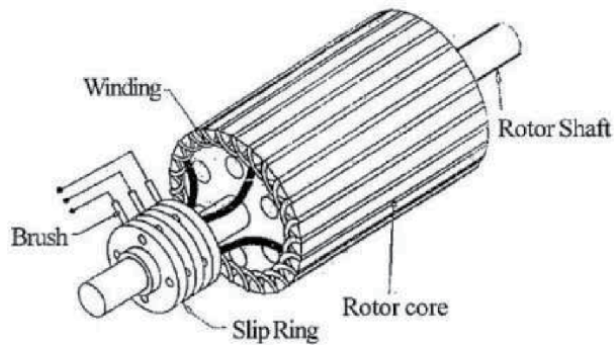
Figure 2.
Squirrel cage rotor.

Figure 3.
Slip ring rotor.

three brushes through which three resistances can be connected in three phase star configuration for reducing starting current and speed control as well as increasing the torque [6]. **Figure 3** shows the slip ring rotor.

3. Classification of IM control strategies

The various IM control techniques are classified in to scalar and vector control methods. The general classification of IM control strategies [8, 9] which are based on the variable frequency control is shown in **Figure 4**.

3.1 Scalar control

The various scalar control methods are as follows 1. Stator voltage control 2. frequency control 3. Voltz/Hertz (V/F) control 4. Rotor Voltage control 5. Changing the number of poles. Out of these scalar methods, V/F control method is the best scalar control method. It can able to adjust the speed of the Induction motor by controlling the amplitude and frequency of the stator voltage of induction motor, the ratio of stator voltage to frequency should be kept constant so that, it is called as V/F control of induction motor drive. The vector control is preferred over scalar control methods due to the following disadvantages of scalar methods 1. Control of
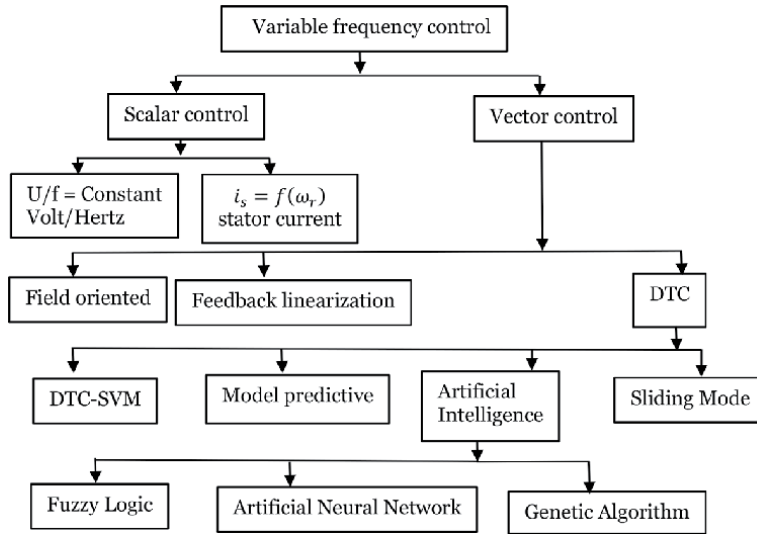
Figure 4.
General classification of control strategies of induction motor.

Voltage/Current/frequency magnitude is based on steady state equivalent circuit model which ignores transient conditions. 2. Coupling of torque and flux exists, and they are functions of frequency and voltage which leads to sluggish dynamic responses [6].

3.2 Vector control methods

3.2.1 Field oriented control (FOC)

The FOC method is implemented based on the analogy of controlling a DC motor. It does not guarantee an exact decoupling of the torque and flux in dynamic and steady state operations. The full information about motor state variable and load torque is required for controlling the IM. The relationship between regulated value and control variables is linear only for constant rotor flux amplitude. The current controllers, coordinate transformations and a PWM algorithm are required. For direct FOC, flux estimator is required. In indirect FOC mechanical speed sensor is needed. This method is very sensitive to rotor time constant.

3.2.2 Direct torque control (DTC)

The DTC is one of the high performance control strategies for the control of AC machine. In a DTC drive applications, flux linkage and electromagnetic torque are controlled directly and independently by the selection of optimum inverter switching modes of operation. To acquire a faster torque output, low inverter switching frequency and low harmonic losses in the model, the selection is made to restrict the flux linkages and electromagnetic torque errors within the respective flux and torque hysteresis bands. The required optimal switching vectors can be selected by using the optimum switching voltage vector look-up table. This can be obtained by simple physical considerations involving the position of the stator-flux linkage space vector, the available switching vectors, and the required torque flux linkage.

The torque is controlled by the stator current component I_{sq} in the classical vector control strategy of FOC according to the Eq. (1)

$$M_e = p_b \frac{m_s}{2} \frac{L_M}{L_r} \Psi_r I_{sq} \tag{1}$$

The motor torque is expressed by rotor flux magnitude Ψ_r and stator current component I_{sq} as given in the Eq. (2) and this equation is written as:

$$M_e = p_b \frac{m_s}{2} \frac{L_M}{L_r} \Psi_r I_s sin\delta \tag{2}$$

The Eq. (2) is transformed into the Eq. (3)

$$M_e = p_b \frac{m_s}{2} \frac{L_M}{L_r L_s - L_m^2} \Psi_s \Psi_r \ sin \ \delta_\Psi \tag{3}$$

where δ is the angle between rotor flux vector and stator current vector and δ_Ψ is the angle between rotor and stator flux vectors. The torque value depends on the magnitude of stator and rotor flux as well as the angle δ_Ψ. For FOC methods, the angle δ is considered whereas angle δ_Ψ is considered for DTC techniques.

The vector diagram of IM is shown in **Figure 5**.

From the motor voltage Eq. (5) for the omitted voltage drop on the stator resistance, the stator flux can be expressed.

From the mathematical model of IM, the electromagnetic torque equation is given in the Eq. (4)

$$M_e = p_b \frac{m_s}{2} \ Im\left(\Psi_s^* I_s\right) \tag{4}$$

Taking into consideration the fact that in the cage motor the rotor voltage equals zero and the electromagnetic torque Eq. (4), the following Eq. (5) is derived.

$$U_{sK} = R_s I_{sK} + \frac{d\Psi_{sK}}{dt} + j\Omega_K \Psi_{sK} \tag{5}$$

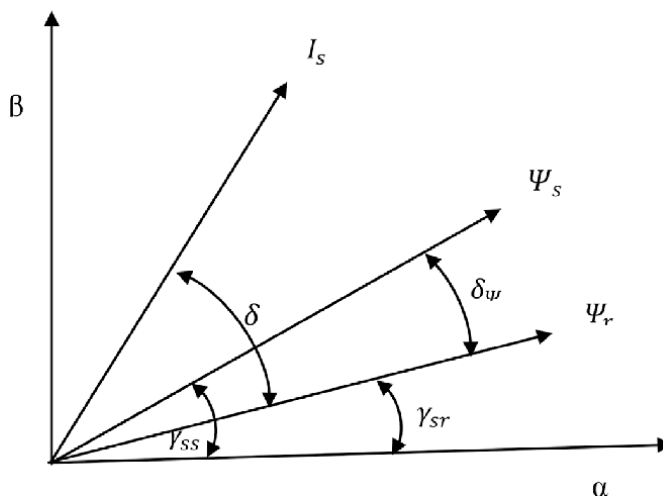$$\frac{d\Psi_s}{dt} = U_s \tag{6}$$

Figure 5.
Vector diagram of induction motor.

Taking into consideration the output voltage of the inverter in the above Eq. (6) it can be written as

$$\Psi_s = \int_0^t U_v dt \tag{7}$$

where

$$U_v = \begin{cases} \dfrac{2}{3} U_{dc} e^{\, j(v-1)\pi/3} & v = 1 \dots 6 \\ 0, \ \dots \ \dots \ \dots \ \dots \ \dots \ \dots & v = 0,7 \end{cases} \tag{8}$$

The Eq. (7) describes eight voltage vectors which correspond to possible inverter states. These vectors are shown in **Figure 6**. There are six active vectors U1 to U6 and two zero vectors U0, U7.

It can be seen from the Eq. (7) that the stator flux directly depends on the inverter voltage Eq. (8). By using one of the active voltage vectors the stator flux vector moves to the direction and sense of the voltage vector. Stator flux changes direction for the cycle sequence of the active voltage vectors. Inherently the rotor flux of IM moves slowly but the stator flux could be changed immediately. In DTC methods the angle δ_Ψ between stator and rotor flux is varied to control the torque. By adjusting the stator voltage, stator flux could be controlled in simple way. The above consideration and equations could be used in the analysis of classical DTC techniques and SVM-DTC methods. In the classical DTC method the control plane is divided for the six sectors shown in **Figure 7**, that are defined as:

$$\gamma_{ss} \in \left(-\frac{\pi}{6}, +\frac{\pi}{6}\right) \tag{9}$$

$$\gamma_{ss} \in \left(+\frac{\pi}{6}, -\frac{\pi}{2}\right) \tag{10}$$

$$\gamma_{ss} \in \left(+\frac{\pi}{2}, +\frac{5\pi}{6}\right) \tag{11}$$

$$\gamma_{ss} \in \left(+\frac{5\pi}{6}, -\frac{5\pi}{6}\right) \tag{12}$$
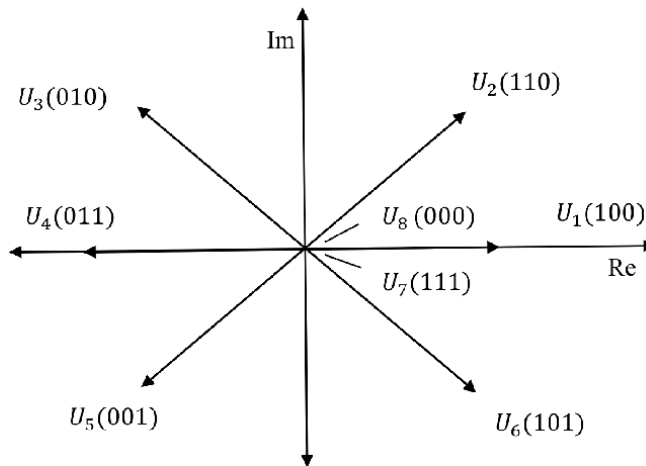

Figure 6.
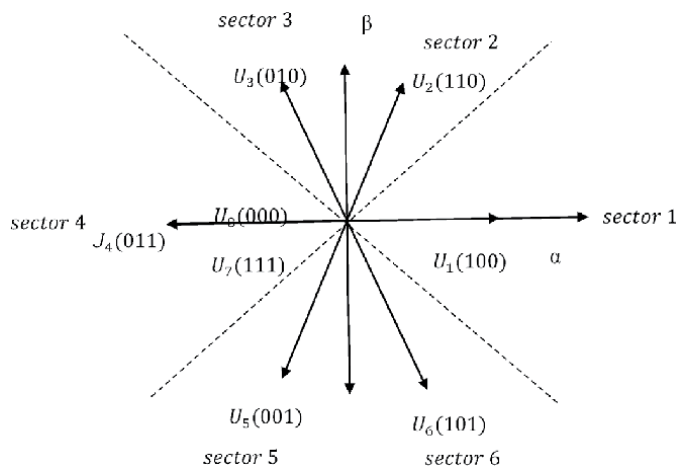*Inverter output voltage represented as space vectors.*

Figure 7.
Sectors in classical DTC.

$$\gamma_{ss} \in \left(-\frac{5\pi}{6}, -\frac{\pi}{2} \right) \tag{13}$$

$$\gamma_{ss} \in \left(-\frac{\pi}{2}, -\frac{\pi}{6} \right) \tag{14}$$

In order to increase magnitude of the stator vector in sector 1, the following voltage vectors $\mathbf{U_1}\ \mathbf{U_2}\ \mathbf{U_6}$ are selected. Conversely to decrease, $\mathbf{U_3}\ \mathbf{U_4}\ \mathbf{U_5}$ are selected. The stator flux is not changed when any one of the zero vectors $\mathbf{U_0}$ or $\mathbf{U_7}$ is applied. The solving of integration in Eq. (7) is stopped.

To increase the motor torque, the voltage vectors $\mathbf{U_2}\ \mathbf{U_3}\ \mathbf{U_4}$ are selected and for decreasing the torque $\mathbf{U_1}\ \mathbf{U_5}\ \mathbf{U_6}$ are selected. The switching **Table 1** is constructed based on the above considerations.

I. Takahashi and T. Nogouchi proposed the control scheme for Direct torque control and it is block diagram is shown in **Figure 8**.

The reference signals such as stator flux amplitude Ψ_{sc} and the electromagnetic torque M_c are compared with the estimated flux amplitude $\hat{\Psi}_s$ and electromagnetic torque $\hat{M}_e$ values respectively. The error values such as e_Ψ and torque e_M are sent to the hysteresis controllers. The appropriate voltage vector from the switching table is selected by the digitized output variables d_Ψ, d_M and the stator flux position sector $\gamma_{ss}(N)$. The power switches in the inverter are controlled by the pulses S_A, S_B, S_C which are generated form the switching table.

According to the Eq. (15) the torque and flux errors are calculated.

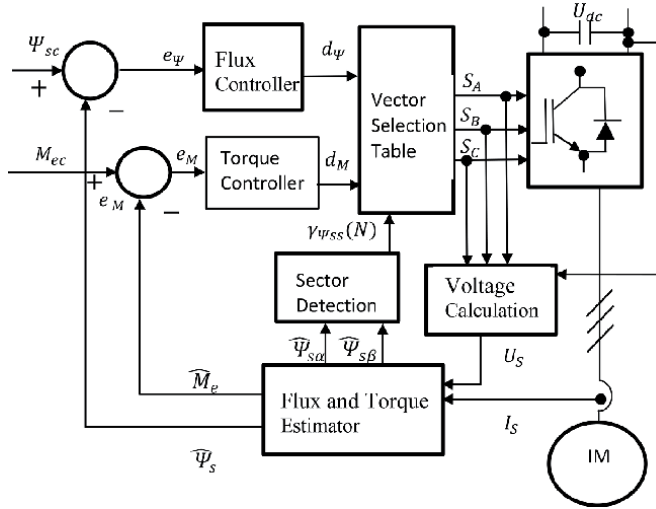| S_Ψ	S_m	S_1	S_2	S_3	S_4	S_5	S_6
1	1	U_2	U_3	U_4	U_5	U_6	U_1
	0	U_7	U_0	U_7	U_0	U_7	U_0
	−1	U_6	U_1	U_2	U_3	U_4	U_5
0	1	U_3	U_4	U_5	U_6	U_1	U_2
	0	U_0	U_7	U_0	U_7	U_0	U_7
	−1	U_5	U_6	U_1	U_2	U_3	U_4

Table 1.
Optimum switching table.

Figure 8.
Block diagram of DTC scheme.

$$\varepsilon_{\Psi_s} = \frac{\hat{\Psi}_s - \Psi_{sc}}{\Psi_{sN}} \, 100\% \tag{15}$$

3.2.3 Problems in conventional DTC

Despite its simplicity and robustness, the conventional DTC control has major drawback. The use of hysteresis controllers causes high ripples in the flux and electromagnetic torque at low speeds. It results in undesirable mechanical vibrations and acoustic noise, and subsequently leads to degradation of the machine performances. Thus the variable switching frequency and current distortions could detoriate the quality of the output power. The negligence in the calculation of stator resistance leads to problems at low speed. Moreover, the practical implementation of nonlinear components of the hysteresis type needs low sampling period. Many DTC strategies are developed based on the principle of instantaneous torque and stator flux regulation in order to rectify the drawbacks of classical DTC. The direct determination of the inverter control signals from the switching table is implemented [9].

4. Types of control strategies for torque ripple reductions in DTC

The DTC control strategies are divided into two groups: 1.Typical 2.Modern control strategies. They are classified into few other control techniques such as space vector modulation (SVM-DTC), modified switching table (m-DTC), Artificial Neural Network controller based (ANN-DTC), Fuzzy Logic controller based (FLC-DTC), Genetic algorithm based (GA-DTC), Model predictive controller based (MPC-DTC), Sliding mode based (SMO-DTC) [9, 10] as shown in **Figure 9**.

4.1 Modified DTC

It covers modification in switching table and/or injection of dithering signals. Few attempts are made to avoid the drawbacks in convention DTC either by implementing dither signal injection method or modified switching table method.
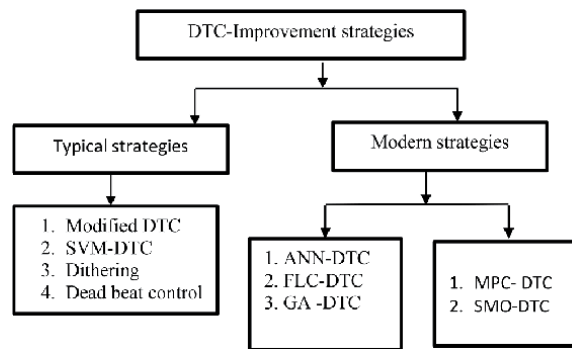
Figure 9.
Classification of DTC improvement strategies.

4.1.1 Modification in switching tables

The modifications are carried out in the DTC- basic switching table with the objective of improving starting and overload conditions which enable all the voltage vectors are applied in appropriate sequence. They are implemented by two methods namely 1. Six sector table and 2. Twelve sector table respectively. The zero voltage vectors are selected from the switching **Table 1** during starting and very low speed conditions and results in flux level reduction due to the drop in stator resistance [11].

4.1.1.1 Modified switching table

4.1.1.1.1 Improvement in switching table

In conventional DTC, the states v1 and v4 vectors are not used. Depending on if the position is in its first 39 degrees or in its second ones, they could increase or decrease the torque. It leads to modify the switching table and use the modified DTC. In the modified DTC, the vectors v3 and v6 are not used. The reason is the ambiguity in flux instead of torque as if it was in conventional DTC [12].

4.1.1.1.2 Modified classical DTC

By applying zero voltage vectors V0, V7 for the states of decreasing in torque, **Table 1** is modified accordingly. The inertia of the motor is reduced when zero voltage vectors are applied, torque ripple is reduced. It is more suitable than the percent given by applying the voltage vectors in **Table 1** for the torque decrease states. **Table 2** illustrates this modification [12].

Voltage vectors	Classical DTC	DTC with changes of zones
V_1	+30° to −30°	0° to −60°
V_2	+90° to +30°	+60° to 0°
V_3	+150° to +90°	+120° to +60°
V_4	−150° to +150°	+180° to +120°
V_5	−90° to −150°	−120° to −180°
V_6	−30°to −90°	−60° to −120°

Table 2.
Modified switching table with 6-sectors.

In both classical DTC and modified DTC there are two states per sector that present a torque ambiguity, so they are never used either. Instead of six sectors, the stator flux locus is divided into twelve sectors. Then all six active states will be implemented per sector. Consequently, the idea of the twelve sector modified DTC [13] is introduced. The tangential voltage vector component is very small and consequently its torque variation will be small as well. Based on this fact, the technique of small torque increase instead of torque increase is implemented [10, 11].

4.1.2 Dither signal injection

Feedback signals should not be delayed in order to maintain maximum possible switching frequency. Due the presence of isolation amplifier, Hall effect transducer and other components, the delay is made inevitably. By introducing the dither signal at very high frequency, the effect due to delay could be compensated. Normally these dither signals are triangular waves at double or triple the sampling frequency of the system. This dithering technique minimizes the torque ripple to 30% compared to conventional DTC method [14].

The frequency of the dither signal is selected well above the cutoff frequency of the system so that its presence could not be detected in the output. When the system parameters are not exactly known and not alterable, the method of instantaneous injection of dither signal is robust to noise in measurements. The inherent delay in signal transduction, data acquisition system and computation leads to low switching frequency which would result in increased torque and flux ripples. The dithering signal injection is implemented to improve the switching frequency of inverter. The appropriate magnitude and frequency of dither signals which are injected in torque and flux errors could minimize torque ripples and acoustic noise level in the drive [15].

4.1.3 Deadbeat control

In the inverter operation to avoid a short circuit in the DC-link, only one switch is turned on at a time. During the transistor switching signals, a delay time must be inserted and as a result the transistors stops to conduct. The dead-time TD is presented for the transistors T_1, T_2 for the two control signals SA+, SA- respectively. Most of the transistors take 1-3 μs duration of dead-time. The safe operation of the inverter is guaranteed by this delay time but it results into a serious distortion in the output voltage. Consequently there is a loss of control momentarily, where a deviation in output voltage from the reference voltage is observed. It is repeated for every switching cycle, so it has significant impact on the control of the inverter and this is known as dead-time effect. The inverter has nonlinear characteristics due to the dead-time and voltage drop on the switching devices. So the compensation algorithms are required in the control strategies [8] as shown in **Figure 10**.

The dead-beat DTC scheme is based on the technique, forcing the magnitude of torque and stator flux to attain their reference values in one sampling period. It is achieved by synthesizing a suitable stator voltage vector applied from Space Vector Modulation (SVM). In this approach the changes in the magnitude of torque and flux over one sampling period are calculated from the motor equations. To get the command value of stator voltage vector in stationary coordinates, a quadratic equation is solved [11].

The flux estimation is crucial part in the sensor less control strategies. The algorithm used for this is sensitive on the calculation accuracy of the inverter output voltage. From the switching signals, the voltages are reconstructed. **Figure 11** shows
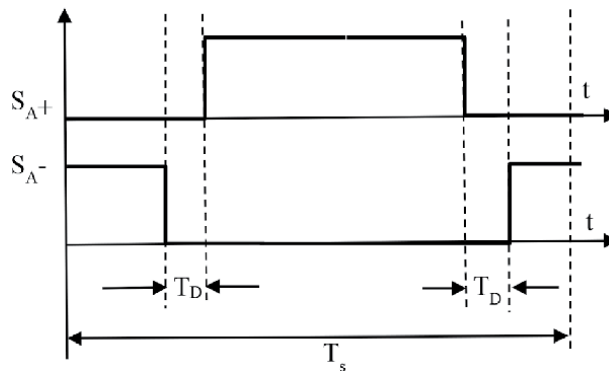
Figure 10.
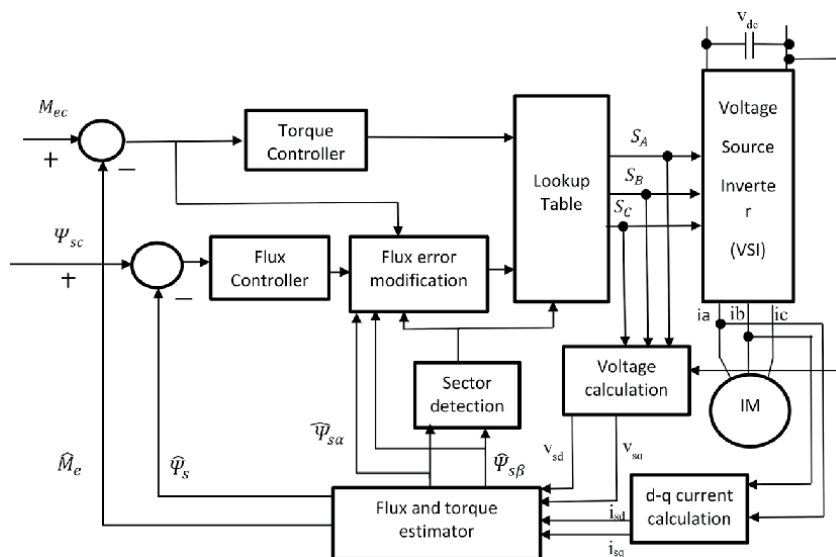*Dead-time effect in PWM inverter.*

Figure 11.
DTC control with modification of flux error status block.

the DTC control with modification of flux error status block [13] dead-time compensation algorithm is significant in this SVM-DTC method [8].

The torque and flux ripple are reduced when the switching frequency of the inverter is maintained constant and greater than the sampling frequency [11].

4.1.3.1 Constant switching frequency approach

For general purpose IM drives, PI-DTC is an appropriate solution in a very wide power range. It is suited to very fast torque and flux controlled drives because of its short sampling time which is required by the switching table DTC schemes [10].

The stator resistance influences the estimation accuracy of stator flux. The characteristics of both torque and flux control loops are affected by error in estimation of stator flux. A new strategy in MATLAB/SIMULINK model is implemented with modified flux error block which resulted in getting quick response [13].

The largest tangential vector to the circular flux locus is produced by an optimized voltage vector. This voltage vector is switched and held to achieve a fast rate

of change of angle Δδsr. The optimized voltage before being it is fed to the lookup table; its selection is done by modifying the flux error status [13].

4.1.4 SVM-DTC

The main difference between classical DTC and DTC-SVM (**Figure 12**) control methods lies in which the control algorithm is being used for the calculations. Based on the instantaneous values, the classical DTC algorithm directly calculates the digital control signals for the inverter. In the DTC-SVM methods control algorithm calculations are based on averaged values whereas the switching signals for the inverter are calculated by space vector modulator. Based on voltage model, the flux estimator with reference flux is selected for the implementation DTC-SVM control structure in sensor less mode of operation [8].

4.1.4.1 SVM

The classical DTC has several disadvantages, among which the variable switching frequency and the high level of ripples are the prominent issues [16]. Further they lead to high-current harmonics and an acoustical noise and they detoriate the control performance at low speeds. The ripples are produced proportionally to the width of the hysteresis band. Due to the discrete nature of the hysteresis controllers, even for the reduced bandwidth values, the ripples are still present [16].

The inverter switching frequency is increased due to even very small values of bandwidths. The modifications in classical DTC strategy is done by including a vector modulator block, which produces space vector PWM technique (SVM) and it is used to implement the voltage vector with a fixed frequency of inverter switching. The switching table and hysteresis controllers are replaced with PI controllers to control the stator flux and the torque [13].

The disadvantages of DTC-SVM with conventional PI controllers are as follows 1. Sensitivity to variation in system parameters and 2. Inadequate rejection of external disturbances and 3. Load changing conditions. These disadvantages are overcome by replacing the conventional PI controllers by intelligent controllers such as adaptive fuzzy-PI or FLC. These intelligent controllers ol more robust against the external disturbances and parameter variations [13].
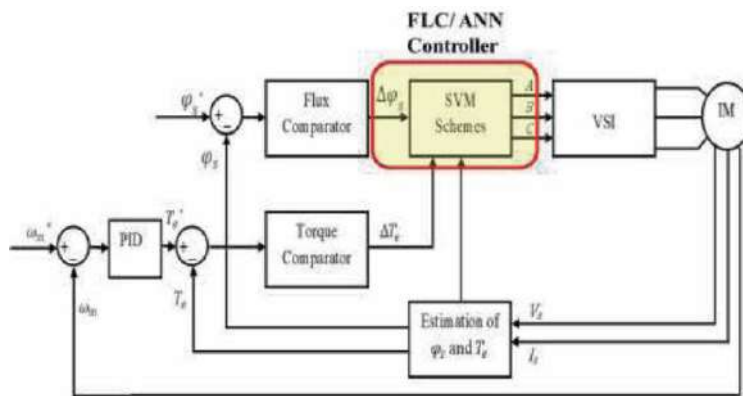

Figure 12.
Block diagram of FLC/ANN controller for DTC-SVM scheme for induction motor.

4.1.4.2 Types of SVM-DTC

The DTC-SVM methods have several following classes namely:

1. PI controllers based DTC-SVM.

2. Predictive/dead-beat based DTC-SVM.

3. Fuzzy logic and/or neural networks based DTC-SVM.

4. Variable-structure control (VSC) [8] based DTC-SVM.

The use of PI controller for torque control of induction motor drives is to overcome an overshoot during startup and to minimize steady state error. The PI controllers provide feedback signals to the system.

In voltage model based stator flux estimation, the pure integrator is replaced with LPF to eliminate the problem of saturation and integration drift due to the DC offsets which are present in the sensed currents or voltages. The LPF introduces the phase and magnitude errors of stator flux estimation which affects the selection of voltages vector and electromagnetic torque response, thereby it deteriorate the performance of DTC drive. To overcome the LPF problems, closed loop of stator flux estimation is implemented [17].

In MRAS, to estimate the rotor speed, PI controller is used and this controller takes more time to tune the proportional and integral gain to obtain the estimated target speed. The MRAS is based on rotor speed, rotor flux and stator current thereby it eliminates the need of PI controller [18].

The effective integration of SVM technique with any n-level multilevel inverter fed DTC drive is achieved by using a fractal based space-vector DTC algorithm. The current THD performance is improved at higher level of DTC drives under transient, steady state and speed reversal operating conditions. Without any significant modification, this strategy could be adapted at any n-level inverter fed DTC controller [19].

4.1.4.3 Proposed artificial intelligent schemes for DTC-SVM

The Space Vector PWM (SVPWM) is a technique used for solving the switching losses in the power converter. The SVPWM is operated in a symmetrical way, so the switching state of each sector is predefined. In this proposed scheme, the initial values to the DTC controller have been fixed based on the induction motor rating. Then the estimation of DTC parameters is found and it is fed to the reference to the Hybrid Asymmetric Space Vector PWM (HASVPWM) controller.

Traditional PWM techniques consist of two signals called carrier signal and reference signal for generating the PWM pulses. If any distortions in the reference signal (i.e error signal) may produce miscellaneous pulses, which will affect the performance of the converter. But SVPWM technique is purely based on estimating the voltage magnitude and its angle for pulse generation. In this, three phase voltages V_{abc} are converted into V_d, V_q and V_0 using abc-dq0 theory. This method will make the estimation of the sector angle and voltage magnitude easier. In traditional SVPWM, each sector denotes 60^0 angles and totally it has six sector and two reference vector in its implementation. Even though the estimation is done for every sector accuracy of generating the pulses is lagging due to the higher range of sector angle and minimum switching sectors. For an example, if estimated sector angle is 55^0, then the switching pattern in sector 1 is selected for the PWM generation. But V_2 vector is also having different switching pattern and that may also well

suited for the same estimated sector angle 55^0. In order avoid such difficult situations, a HASVPWM is used for controlling the DTC drive which reduces torque ripples, switching losses and improved power quality.

The implementation of HASVPWM is similar to the SVPWM technique. In general, three phase Voltage source inverters (VSI) have eight distinct switching losses, where state 1 to 6 are active states, 0 and 7 are inactive switching states. In HASVPWM, asymmetric voltage vectors are represented as V_{ni}, V_{nj} and V_{nk} where n = 1,2,3,4,5,6 and four quadrants. HASVPWM has two non-zero vectors (V_1 and V_2) and two zero vectors (V_0 and V_{24}) in each vector will be used for the vector 15^0. Hence this HASVPWM have 24 sectors and it is shown in **Figure 13**.

Major portion in HASVPWM is to removal of mismatching pulses which will be done by comparing the HASVPWM pulses with the traditional SVPWM pulse. The mismatching pulses are removed by calculating its rise time (T_r) and fall time (T_f) of the mismatching pulses with magnitude. Then the same magnitude of pulse with same instant is added. For mismatching pulse removal. This logic avoids the mismatching pulses in the output and reduce the switching losses in the VSI based DTC drive. In this proposed system, intelligent control methods such as Fuzzy Logic Control (FLC) and Artificial Neural Network (ANN) are utilized to find the suitable sector for continuous operation. They are also efficient than the classical control techniques which are utilized to find suitable sector for the continuous operation.

4.1.4.3.1 Fuzzy logic controller for HASVPWM

The proposed hybridization process is performed by the combination of continuous ASVPWM and fuzzy operated Discontinuous ASVPWM technique. Finally, the mismatching pulses of both PWM techniques are applied to control the inverter. Pulse mismatching technique helps to reduce the active region of the switch and achieve the optimal input pulse to the inverter. Pulse mismatching technique helps to reduce the active region of the switch and achieve the optimal input pulse to the inverter. The optimal hybrid pulse reduces transition time of inverter switch and improves operating performance of the inverter. The Fuzzy rules help to select the optimal switching sector for discontinuous modulation. If there is more number of sectors in the hexagon, it allows more degrees of freedom which help to find the optimal reference voltage and angle. The Fuzzy logic system describes to what degree the rule applies, while the conclusion assigns a fuzzy function to each of one or more output variables. These Fuzzy Expert Systems allow more than one conclusion per rule.
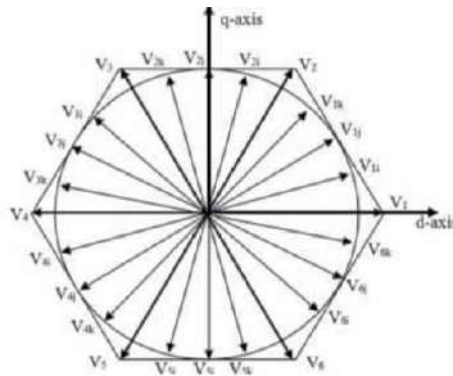

Figure 13.
Structure of HASVPWM hexagon.

CE\E	NB	NS	ZE	PS	PB
NB	NB	NB	NS	NS	ZE
NS	NB	NS	NS	ZE	PS
ZE	NS	NS	ZE	PS	PS
PS	NS	ZE	PS	PS	PB
PB	ZE	PS	PS	PB	PB

Table 3.
Fuzzy Logic Rules to select suitable sector in HASVPWM.

The linguistic labels are divided into five groups. They are: NB-Negative Big; NS- Negative Small; ZE-zero; PS-Positive Small; PB-Positive Big. Each of the inputs and the output contain membership functions with all these five linguistics.

The set of rules in a fuzzy expert system is given in **Table 3** and corresponding input and membership function values are indicated in **Figure 8**.

The simulation model of DTC with HASVPWM scheme is developed using MATLAB software Simulink tool. The fuzzified inputs and defuzzified outputs are shown in **Figures 14–16** respectively. Consider a case, when the sector angle estimated from the SVPWM calculation as shown in **Figure 14** is equal to -165^0, it means negative big (NB) as mentioned in **Table 3**. And change in the sector angle at the next instant is about -110^0, it represent the negative small (NS). Then the corresponding fuzzy output is NB, which is mentioned in **Figure 16**.

4.1.4.3.2 Artificial neural network controller for HASVPWM

The DTC control can also be achieved with HASVPWM using Artificial Neural Network (ANN) control. ANN is nonlinear model that is easy to use and understand compared to statistical methods like Fuzzy logic. Compare with Fuzzy Logic, ANN has an ability to learn from the previous trained data. Hence, the major advantage of
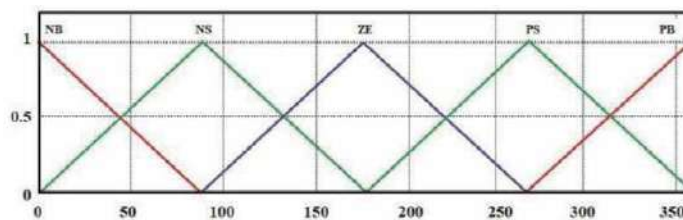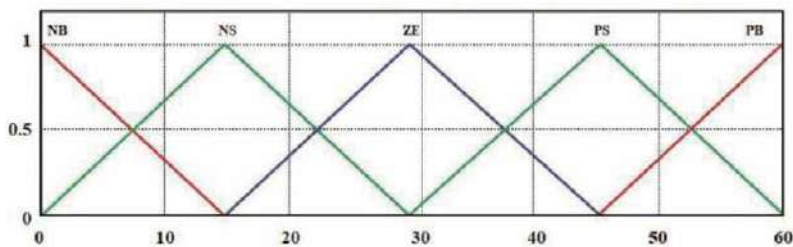

Figure 14.
Degree input to FLC.

Figure 15.
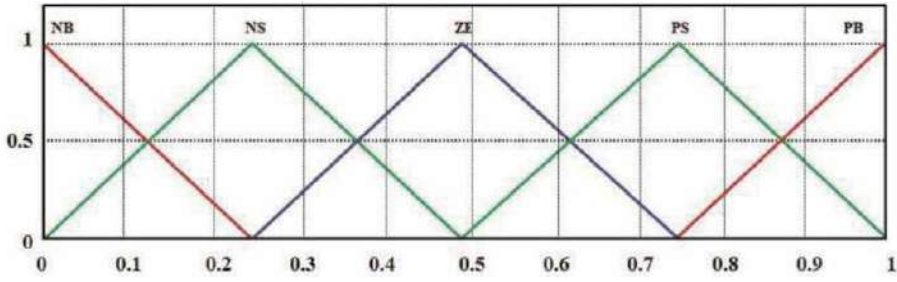*Change in degree error input to FLC.*

Figure 16.
Fuzzy output Modulation index for HASPWM.

ANN is to train a system with large amount of data sets. The output performance will depend upon the trained parameters and the data set relevant to the training data. In this proposed scheme, ANN is used to estimate the suitable sector of HASVPWM.

ANN is used to determine the sector number for the estimated value of θe. There are total of 24 sectors, each sector of 15 degree. Again three layers of neurons are used but with a 5–4-1 feed forward configuration as shown in **Figure 17**. The Input layer is of log sigmoid transfer function, hidden layer is of hyperbolic tangent sigmoid function and the output layer is of linear transfer function. Levenberg - Marquardt back propagation based training method is used for train the neurons. As soon as the training procedure is over, the neural network gives almost the same output pattern for the same or nearby values of input. This tendency of the neural networks which approximates the output for new input i.e. angle theta since sector selection is purely based on theta.

The following **Figure 17** shows the structure of Neural Network (NN) which is utilized in the proposed ANN controller for DTC-SVM scheme for induction motor.

The Step by step procedure for NN Algorithm is given below:

Step 1: Initialize the input weight for each neuron.

Step 2: Apply the training dataset to the network. Here X is the input to the Network and Y_1, Y_2 and Y_3 are the output of the network.

Step 3: Adjust the weights of all neurons.

Step 4: Determine Sector Angle for SVPWM.

Compare with Fuzzy logic control, ANN control in HASVPWM is able to identify the suitable voltage vector and its angle for minimizing the torque ripple and PEC losses and THD, maximizing DTC capabilities under various operating conditions like speed reversal, loading conditions etc. The effectiveness of ANN-HASVPWM in DTC scheme is predicted by comparing ANN with the Fuzzy based
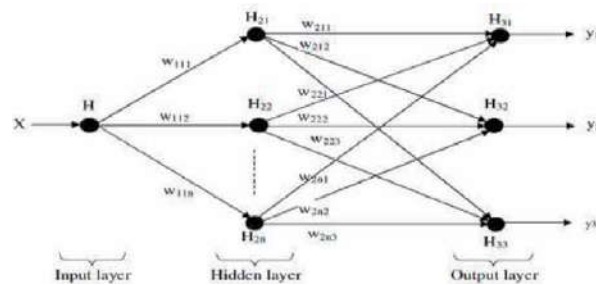

Figure 17.
The structure of network utilized in the proposed technique.

Control strategies	Torque ripple factor (%)
Proposed FLC controller for HASVPWM FOR DTC-SVM scheme	**5.1**
Proposed ANN controller for HASVPWM FOR DTC-SVM scheme	**4.5**

Table 4.
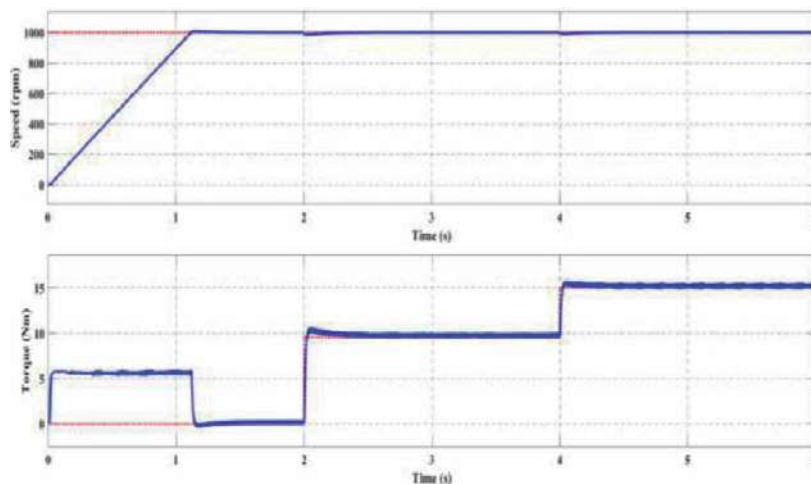*Comparison of control strategies in induction motor.*

Figure 18.
Speed and torque output for FLC based DTC-SVM of IM with HASVPWM.

HASVPWM scheme. The results for ANN based HASVPWM scheme to DTC controller under the same loading conditions, it shows that torques ripple, switching loss and harmonic content reduction is expected. The comparative simulation results are clearly presented and shown in **Table 4**.

4.1.4.3.3 Simulation results and discussion

The two proposed schemes namely 1.Fuzzy Logic Controller (FLC) for DTC-SVM and 2.Artificial Neural Network (ANN) controller for DTC-SVM respectively for IM. Has been simulated using MATLAB version R2009a and the results are compared and shown in **Table 4**. Both of the proposed scheme methods uses HASVPWM. The parameters of IM used in the simulation are given in the appendix.

The torque ripple can be calculated by using the relation.

$$\text{Torque Ripple Factor} = (\text{Peak to Peak torque})/\text{Rated torque} \qquad (16)$$

The simulation results of FLC for DTC-SVM of IM with HASVPWM is shown in **Figures 18** and **19**.The simulation results of ANN for DTC-SVM of IM with HASVPWM is shown in **Figures 20** and **21**.

From **Figure 19** (Torque ripple waveform) it is inferred that the torque ripples oscillates from 9.5 Nm (Minimum) to 10.1 Nm (maximum) for the given Reference torque of 10 Nm.

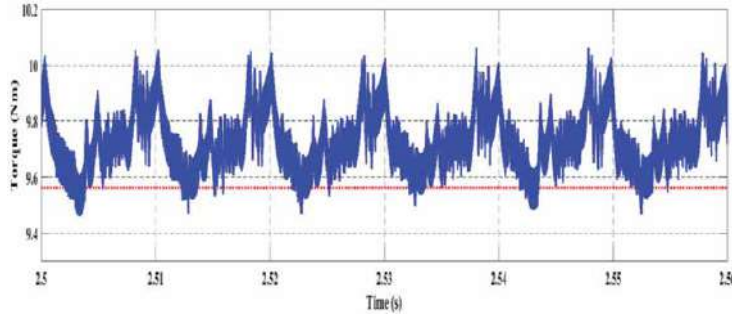Torque Ripple factor (%) as per Eq. 23 is given by = $((10.01–9.5)/10) \times 100 = 0.51/10 \times 100 = $ **5.1.**

Figure 19.
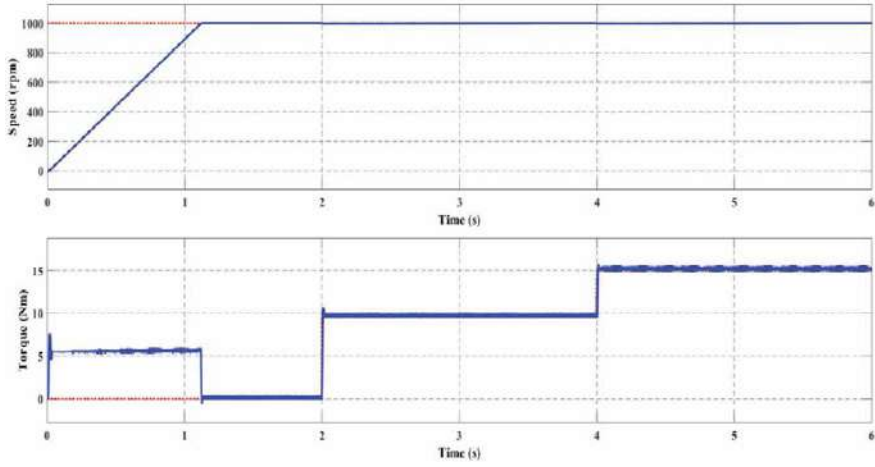*Torque ripples for FLC based DTC-SVM of IM with HASVPWM.*

Figure 20.
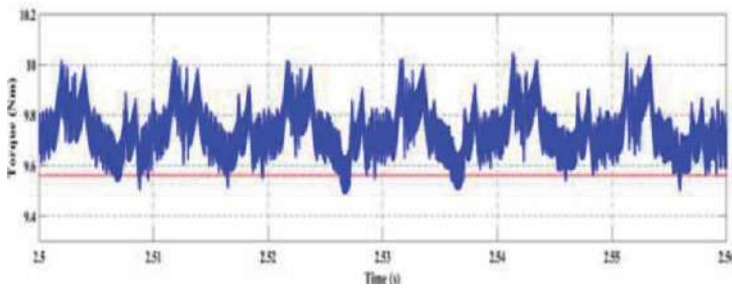*Speed and torque output for ANN based DTC-SVM of IM with HASVPWM.*

Figure 21.
Torque ripples for ANN based DTC-SVM of IM with HASVPWM.

From **Figure 21** (Torque ripple waveform) it is inferred that the torque ripples oscillates from 9.55 Nm (Minimum) to 10 Nm (maximum) for the given Reference torque of 10 Nm.

Torque Ripple factor (%) as per Eq. 23 is given by = ((10–9.55)/10) × 100 = 0.45/10×100 = **4.5.**

Figure 22 shows the comparison of Torque Ripple of FLC and ANN based DTC-SVM of IM with HASVPWM at 1000 rpm.
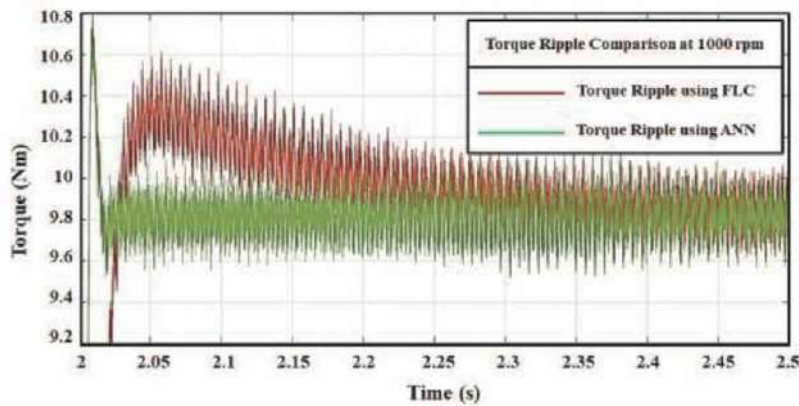
Figure 22.
Torque ripple comparison of FLC and ANN based DTC- SVM of IM with HASVPWM.

It is clear that variation in Torque ripples shown in **Table 4** is less in case of ANN and they can achieve a minimum torque ripple than other control techniques. It has been viewed that the discussed control strategy has helped in reducing the torque ripples. Thus, by using FLC and ANN based controller for DTC of IM, the ripples are reduced completely.

5. Modern strategies of DTC

5.1 Fuzzy logic control (FLC)

The limits of the torque hysteresis band are controlled by FLC. It entails a minimization of the torque ripples as well as an improvement of the dynamic performances of IM. The FLC selects the optimum bandwidth of the torque hysteresis in real time [9].

The fuzzified parameters such as torque error, stator flux errors, and stator flux angle are the input to FLC. The switching state of the inverter is a crisp value obtained as an output from the FLC [11].

A detailed classification and comparison of DTC strategies like SMC, FLC and ANN in terms of performance parameters of induction machine were discussed in [20].

The PI controller and FLC algorithm have been implemented for the three-phase induction motor and it is found that the proposed FLC scheme is better than the conventional DTC control with PI control in [21].

The effective DTC improvements are achieved by Fuzzy logic controller thereby the ripples in torque and flux are reduced, consequently secondary problems for the motor such as heating, mechanical vibration, aging are also rectified. The merits of the conventional are also preserved [22].

5.2 Artificial neural network (ANN)

A multilayer ANN allows to replace both hysteresis comparators and the selection table in classical DTC.

The ANN offers the following merit over classical DTC.

    i. The complexity of the controller is reduced;

   ii. The effects of motor parameter variations are minimized.

   iii. The controller time response is improved.

   iv. The robustness of drive is improved [11].

   For electric vehicle applications, the FLC and ANN based monitoring systems for the DTC controlled induction motor drive was implemented to detect a very small change in performance parameters [23].

Acknowledgements

Nomenclature

f_c	crossover frequency
i_d	d-axis current
L_{dm}	d-axis magnetizing inductance
L_d	d-axis self-inductance
V_d	d-axis voltage
ρ	derivative operator
T_e	develop electromagnetic torque
d	direct or polar axis
DTC	direct torque control
ω_r	electrical speed
i_f	equivalent permanent magnet field current
L_s	equivalent self-inductance per phase
λ_d	flux linkage due d axis
λ_q	flux linkage due q axis
λ_{dm}	flux linkage due to rotor magnets linking the stator
B	friction
FLC	fuzzy logic controller
J	inertia
k_i	integral control gain
T_L	load torque
ω_{rated}	motor rated speed
T_m	motor torque
P	number of poles
I_m	peak value of supply current
λ_f	PM flux linkage or field flux linkage
k_p	proportional control gain
i_q	q-axis current
L_{qm}	q-axis magnetizing inductance
L_q	q-axis self-inductance
V_q	q-axis voltage
q	quadrature or interpolar axis

T_{ref}	reference motor torque
θ_r	rotor position
ω_m	rotor speed
L	self-inductance
L_{ls}	stator leakage inductance
R_s	stator resistance
i_a, i_b, i_c	three phase currents
V_a, V_b, V_c	three phase voltage

A. Appendices

A.1 Appendix 1: parameters of 3 phase squirrel cage induction motor

RATED POWER	5.4 HP
RATED VOLTAGE	400 V
RATED SPEED	1430 RPM
RATED TORQUE	26.7 Nm
RATED CURRENT	8.5 A
STATOR RESISTANCE	1.405 Ω
ROTOR RESISTANCE	1.395 Ω
STATOR INDUCTANCE Ls	0.005839H
ROTOR INDUCTANCE Lr	0.005839H
MAGNETIC FLUX	0.1827 weber
NO. OF POLES	4
MOMENT OF INERTIA	0.0131 kgm^2
FRICTION FACTOR	0.002985 Nms/rad

Author details

Adhavan Balashanmugham[1*], Maheswaran Mockaisamy[2]
and Sathiyanathan Murugesan[1]

1 Department of Electrical and Electronics Engineering, PSG Institute of
Technology and Applied Research, Coimbatore, Tamil Nadu, India

2 Department of Mechatronics Engineering, Nehru Institute of Engineering and
Technology, Coimbatore, India

*Address all correspondence to: adhav14@gmail.com

IntechOpen

References

[1] Takahashi, Noguchi T. A new quick response and high-efficiency control strategy of an induction motor. IEEE Transactions on Industry Applications., Vol.22, No.5, pp.820–827, 1986. DOI: 10.1109/TIA.1986.4504799

[2] Depenbrock M. Direct self control (DSC) of inverter fed induction machine. IEEE Transactions on Power Electronics. 1988; 3(4):420–429. DOI: 10.1109/63.17963

[3] Ben Salem, F. and Derbel N., 'Direct torque control of induction motors based on discrete space vector modulation using adaptive sliding mode control', International Journal of Electric Power Components and Systems, 2014, 42, (14), pp. 1598–1610.

[4] F. Ben Salem and N. Derbel, 'Performance Analysis of DTC-SVM Sliding Mode Controllers-Based Parameters Estimator of Electric Motor Speed Drive', Mathematical Problems in Engineering, Volume 2014, Article ID 127128, http://dx.doi.org/10.1155/2014/127128, 2014.

[5] Ben Salem,F. and Derbel,N., 'DTC-SVM Based Sliding Mode Controllers with Load Torque Estimators for Induction Motor Drives', Chapter 14 of the Book: Applications of Sliding Mode Control, Studies in Systems, Decision and Control 79, Springer Science+ Business Media Singapore 2017, pp. 269–297

[6] P.C. Krause,O. Wasynczuk, S. D. Sudhoff "Analysis of Electric Machinery and Drive Systems", IEEE Press, A John Wiley & Sons, Inc. Publication Second Edition, 2002.

[7] H. C. Stanley, "An Analysis of the Induction Motor", AIEE Transactions, Vol. 57 (Supplement), pp. 751–755, 1938.

[8] Marcin Żelechowski. Space Vector Modulated – Direct Torque Controlled

(DTC–SVM) Inverter–Fed Induction Motor Drive, Dissertation, Warsaw University of Technology; Warsaw, 2005. p. 1–175.

[9] Najib El Ouanjli et al. Modern improvement techniques of direct torque control for induction motor drives - a review. Protection and Control of Modern Power Systems. Springer Open; 2019. p. 1–12. https://doi.org/10.1186/s41601-019-0125-5.

[10] Vojkan Kostić et al. Expermental Verification of Direct Control Methods for Electric Drive Application. Facta Universitatis. Series: Automatic Control and Robotics; Vol. 8, No.1, 2009. pp. 111–126.

[11] M.Vasudevan. Improved Direct Torque Control Strategy with Ripple Minimization for Induction motor drive. Anna University: Chennai; 2006. p. 39–87.

[12] Eng.Ahmed Hassan Adel et al. Torque Ripple Reduction in Direct Torque Control of Induction Motor Drives by Improvement of the Switching Table. Journal of Multidisciplinary Engineering Science and Technology; Vol. 1 Issue 5, 2014. p. 1–6.

[13] Madhuri D. Kulkarni, Vivek D. Bavdhane. Quick Dynamic Torque Control in DTC-Hysteresis-Based Induction Motor by Using New Optimized Switching Strategy. International Journal of Innovations in Engineering Research and Technology; Vol. 2, Issue 7, 2015. p. 1–11.

[14] Jaya N. Tattea, Mohoda, S. B. Performance Improvement of Induction Motor by Using Direct Torque Control Technique. International Journal of Development Research; Vol. 07, Issue 10, 2017. pp.15901–15905.

[15] RK.Behra, SP.Das Improved direct torque control of induction motor with dither injection, Sadhana; Vol. 33, Part 5, 2008. p. 551–564.

[16] Cherifi Djamila, Miloud Yahia. Direct Torque Control Strategies of Induction Machine: Comparative Studies. Direct Torque Control Strategies of Electrical Machines. Intechopen p. 1–23. DOI: http://dx.doi.org/10.5772/intechopen.90199.

[17] Rajendran R. Certain Investigations and Realization of SVM-DTC of Induction Motor Drives Using FPGA. Anna University, Chennai; 2012. p. 46–66.

[18] Hassan Farhan Rashag et al. DTC-SVM Based on PI Torque and PI Flux Controllers to Achieve High Performance of Induction Motor. Research Journal of Applied Sciences, Engineering and Technology 7(4); 2014. p. 875–891.

[19] Vinod B. R., Shiny G. A Multilevel Inverter fed Direct Torque Control Strategy for an Induction Motor using PI Controllers. International Journal of Engineering and Advanced Technology; Volume-7 Issue-4, 2018. p. 90–99.

[20] Najib El Ouanjli et al. Modern Improvement Techniques of Direct Torque Control for Induction Motor Drives - A review, Protection and Control of Modern Power Systems. 2019, 4:11,https://doi.org/10.1186/s41601-019-0125-5, pp. 1–12.

[21] J. Jeyashanthi, M. Santhi. Performance of Direct Torque Controlled Induction Motor Drive by Fuzzy Logic Controller. CEAI; Vol.22, No.1, 2020, pp. 63–71.

[22] Najib El Ouanjli et al. Improved DTC strategy of doubly fed induction motor using fuzzy logic controller. Elsevier Energy Reports 5, 2019, pp. 271–279.

[23] Abarna J, Velnath R. Modeling of Three Phase Induction Motor with DTC Drive Fault Analysis using Fuzzy Logic. International Journal of Recent Technology and Engineering (IJRTE); ISSN: 2277–3878, Vol. 9, Issue-1, May 2020. pp. 1196–1202.

Edited by Fatma Ben Salem

This book deals with the design and analysis of Direct Torque Control (DTC). It introduces readers to two major applications of electrical machines: speed drive and position control and gives the readers a comprehensive overview of the field of DTC dedicated to AC machines. It includes new DTC approaches with and without control of commutation frequency. It also covers DTC applications using artificial intelligence. The book combines theoretical analysis, simulation, and experimental concepts.To make the content as accessible as possible, the book employs a clear proposal in each chapter, moving from the background, to numerical development, and finally to case studies and illustrations. The book is a wide-ranging reference source for graduate students, researchers, and professors from related fields and it will benefit practicing engineers and experts from the industry.

IntechOpen